frontmatter/fig/USlogo-top.pdf

A Multiplexed Impedance Analyser for Biosensing Applications

Karl Voigt

24867209

Report submitted in partial fulfilment of the requirements of the module
Project (E) 448 for the degree Baccalaureus in Engineering in the Department of
Electrical and Electronic Engineering at Stellenbosch University.

Supervisor: Dr T. Ebrahim

October 2025

Acknowledgements

I would like to thank my dog, Muffin. I also would like to thank the inventor of the incubator; without him/her, I would not be here. Finally, I would like to thank Dr Herman Kamper for this amazing report template.

frontmatter/fig/USlogo-top.pdf

Plagiaatverklaring / *Plagiarism Declaration*

1. Plagiaat is die oorneem en gebruik van die idees, materiaal en ander intellektuele eiendom van ander persone asof dit jou eie werk is.
   Plagiarism is the use of ideas, material and other intellectual property of another's work and to present is as my own.

2. Ek erken dat die pleeg van plagiaat 'n strafbare oortreding is aangesien dit 'n vorm van diefstal is.
   I agree that plagiarism is a punishable offence because it constitutes theft.

3. Ek verstaan ook dat direkte vertalings plagiaat is.
   I also understand that direct translations are plagiarism.

4. Dienooreenkomstig is alle aanhalings en bydraes vanuit enige bron (ingesluit die internet) volledig verwys (erken). Ek erken dat die woordelikse aanhaal van teks sonder aanhalingstekens (selfs al word die bron volledig erken) plagiaat is.
   Accordingly all quotations and contributions from any source whatsoever (including the internet) have been cited fully. I understand that the reproduction of text without quotation marks (even when the source is cited) is plagiarism

5. Ek verklaar dat die werk in hierdie skryfstuk vervat, behalwe waar anders aange-dui, my eie oorspronklike werk is en dat ek dit nie vantevore in die geheel of gedeeltelik ingehandig het vir bepunting in hierdie module/werkstuk of 'n ander module/werkstuk nie.
   I declare that the work contained in this assignment, except where otherwise stated, is my original work and that I have not previously (in its entirety or in part) submitted it for grading in this module/assignment or another module/assignment.

Studentenommer / *Student number*	Handtekening / *Signature*
Voorletters en van / *Initials and surname*	Datum / *Date*

Abstract

English

The English abstract.

Afrikaans

Die Afrikaanse uittreksel.

Contents

List of Figures

List of Tables

Nomenclature

Variables and functions

$p(x)$	Probability density function with respect to variable x.
$P(A)$	Probability of event A occurring.
ε	The Bayes error.
ε_u	The Bhattacharyya bound.
B	The Bhattacharyya distance.
s	An HMM state. A subscript is used to refer to a particular state, e.g. s_i refers to the ith state of an HMM.
$\mathbf{S}$	A set of HMM states.
$\mathbf{F}$	A set of frames.
$\mathbf{o}_f$	Observation (feature) vector associated with frame f.
$\gamma_s(\mathbf{o}_f)$	A posteriori probability of the observation vector $\mathbf{o}_f$ being generated by HMM state s.
μ	Statistical mean vector.
Σ	Statistical covariance matrix.
$L(\mathbf{S})$	Log likelihood of the set of HMM states $\mathbf{S}$ generating the training set observation vectors assigned to the states in that set.
$\mathcal{N}(\mathbf{x}|\mu, \Sigma)$	Multivariate Gaussian PDF with mean μ and covariance matrix Σ.
a_{ij}	The probability of a transition from HMM state s_i to state s_j.
N	Total number of frames or number of tokens, depending on the context.
D	Number of deletion errors.
I	Number of insertion errors.
S	Number of substitution errors.

Acronyms and abbreviations

ADC analogue-to-digital converter

BLE Bluetooth Low Energy

CPE constant phase element

DAC digital-to-analogue converter

DMA direct memory access

DSP digital signal processing

DUT device-under-test

EIS electrochemical impedance spectroscopy

EMI electromagnetic interference

FFT fast Fourier transform

FPU floating point unit

GBW gain-bandwidth product

GPIO general-purpose input/output

HCW healthcare worker

IC integrated circuit

IDE interdigitated electrode

LDO low-dropout regulator

LPF low-pass filter

MCU microcontroller unit

NFC near-field communication

PCB printed circuit board

PGA programmable gain amplifier

POC point-of-care

TIA transimpedance amplifier

Chapter 1

Introduction

1.1. Background

Biosensors are devices that measure biological and chemical reactions through physical transducer mechanisms, generating signals proportional to the concentration of an analyte in a sample [1]. This enables detection of biomarkers that can be used to monitor health conditions or diagnose diseases [2]. Early disease screening using biosensors could provide significant healthcare benefits, particularly in resource-limited settings [3].

Commercial impedance analysers for biosensing, such as the PalmSens4, offer exceptional technical capabilities but are prohibitively expensive (approximately R85 000) and require substantial technical expertise to interpret electrochemical impedance spectroscopy (EIS) data. This creates a significant barrier to adoption in point-of-care (POC) environments, particularly in rural clinics and community health facilities where specialized personnel and equipment may be unavailable [4].

Designing a low-cost, easy-to-use device to perform impedance measurements on interdigitated electrodes (IDEs), developed through previous research at this institution, would provide a valuable tool for POC disease screening. By abstracting the complexity of EIS interpretation and presenting results in an intuitive format, such a device would enable healthcare workers without specialized training to identify patients requiring further testing or specialist referral [4]. Furthermore, a multiplexed system capable of measuring multiple IDEs from a single sample would improve efficiency and reduce the need for repeated sample collection, making screening more practical in high-volume POC settings [4].

1.2. Project Objectives

This project aims to develop a low-cost, user-friendly multiplexed impedance analyser for biosensing applications. The system design objectives include:

1. Developing analogue frontend circuitry that enables microcontroller-based IDE measurements using electrochemical impedance spectroscopy (EIS), including excitation signal generation, voltage measurement, and current measurement stages.

2. Implementing multiplexing capability to sequentially measure up to four IDE without manual intervention.

3. Designing and fabricating a printed circuit board (PCB) that integrates all analogue and digital subsystems.

4. Developing firmware for signal processing and impedance calculation.

5. Creating an intuitive user interface that enables device operation across diverse point-of-care settings by healthcare workers (HCWs) without requiring external equipment or specialized knowledge.

6. Ensuring the complete system is battery-powered, portable, and achieves a total cost under R4,500 to enable widespread adoption.

7. Calibrating and validating the system against a commercial reference instrument (PalmSens4) using test cells and IDE measurements.

1.3. Project Scope

This project focuses on the development of a multiplexed impedance analyser system for biosensing applications. The scope includes:

1.3.1. Inclusions

- Design and implementation of analogue frontend circuitry for electrochemical impedance spectroscopy (EIS) measurements

- Development of signal generation, voltage measurement, and current measurement stages

- Integration of multiplexing capability to sequentially measure up to four biosensors

- Design and fabrication of a printed circuit board (PCB) for the complete system

- Firmware development for the STM32 measurement subsystem and ESP32 user interface

- Implementation of both on-device (LCD and buttons) and web-based user interfaces

- System calibration and validation using passive test cells and phosphate buffered saline (PBS) solutions

- Demonstration of surface-based protein binding detection using bovine serum albumin (BSA)

1.3.2. Exclusions

- Design and fabrication of IDEs (existing IDEs from prior research are used)

- Imobilisation of biological recognition elements (e.g., antibodies) on the IDEs and antigen-antibody binding experiments

- Testing with blood samples or patient specimens (requires medical laboratory certification and ethical approval)

- Clinical validation studies with real disease biomarkers

1.4. Chapter Overview

Chapter 1: Introduction

Provides the background, motivation, objectives, and scope of the project, outlining the need for low-cost, user-friendly impedance analysers for point-of-care biosensing applications.

Chapter 2: Literature Review

Reviews the fundamental principles of biosensors, electrochemical impedance spectroscopy, impedance analyser architectures and related work in portable EIS systems.

Chapter 3: Design

Details the complete system design process, including the design philosophy, analogue frontend development, multiplexer implementation, PCB design considerations, firmware architecture, and circuit simulation validation.

Chapter 4: Testing & Validation

Presents the systematic testing and validation methodology, progressing from individual subsystem characterization through complete system integration. Includes calibration procedures, measurements with PBS solutions of varying concentrations, and BSA protein binding validation experiments comparing BioPal performance against the PalmSens4 reference instrument.

Chapter 5: Summary and Conclusion

Summarizes the project outcomes, discusses the BioPal's performance characteristics across different frequency ranges, and evaluates its suitability for point-of-care biosensor applications.

Chapter 2

Literature Review

This chapter establishes the theoretical foundation for developing a impedance analyser for POC biosensing applications. The fundamental principles of biosensors and electrochemical impedance spectroscopy are examined, followed by an analysis of impedance measurement techniques and existing instrumentation approaches. This review identifies key design considerations and trade-offs that inform the development of a practical point-of-care impedance measurement system.

2.1. Background on Biosensors

Biosensors are employed in applications such as disease monitoring, drug discovery, and detection of pollutants, disease-causing micro-organisms and markers that are indicators of a disease in bodily fluids (blood, urine, saliva, sweat) [1].

A biosensor consists of an analyte, a bioreceptor and a transducer mechanism combined with the electronics needed to process the signal [1]. The analyte is the substance of interest that needs detection. When the analyte is a subtance that acts as an objective measure that that gives an indication of the biological processes happening inside the body at a given moment, they are reffered to as biomarkers [2]. Bioreceptors are molecules such as enzymes, cells, DNA or antibodies that specifically recognise and interact with the analyte. They produce a signal (in the form of light, heat, pH, charge or mass change, etc.) when they interact with the biomarker [1].

Many biosensors require that a "label" is attached to the biomolecule of interest and then the concentration of this label is detected and extrapolated to the concentration of the biomolecule [5]. Label-free biosensors, on the other hand, directly detect the target biomolecule by measuring the changes in electrical properties of the surface of the biosensor when binding occurs. Since labelling can dramatically alter the binding properties of biomolecules and adds complexity and cost to the assay process, label-free detection is highly desirable [5], especially in point-of-care environments. The IDE's used for testing in this project use antibodies as the label-free bio-recognition element.

The concentration of the analyte in the sample can be estimated based on the number of bio-recognition events, however in order to convert the bio-recognition events into a

measurable signal, a transducer mechanism is needed [1].

2.1.1. Transducer Mechanisms

There are various types of transducer mechanisms that can be used in biosensors, including optical, piezoelectric and electrochemical transducers. This project will focus on biosensors where binding events change the electrical properties of the biosensor, specifically the complex impedance. Thus, electrochemical transducers are of interest.

Electrochemical transducers can use various analysis techniques. In potentiometric analysis, the potential of an electrode is measured against a reference electrode at zero-current [6]. Coulometry applies a constant potential (with regard to a reference electrode) onto an electrode surface to carry out exhaustive electrolysis of an analyte [6]. Voltammetry involves subjecting the sample to a varying potential at the electrode's surface and measuring the resulting Faradaic current [6]. Finally, there is electrochemical impedance spectroscopy (EIS), which measures the complex impedance of an electrochemical system as a function of frequency [6]. EIS is particularly suitable for biosensor applications where biological binding events alter the electrical properties of the electrode-electrolyte interface [5].

2.2. Fundamentals of EIS

EIS involves applying a small sinusoidal perturbation to the device-under-test (DUT) and measuring the response. This can be either a voltage or current signal, while the other is measured. By varying the frequency of the excitation signal, different electrochemical processes that occur at distinct time constants can be characterised.

EIS relies on the system acting as a linear time-invariant system, but most real-world electrochemical systems are inherently nonlinear [7]. To approximate linear behaviour and ensure valid results, EIS uses a small AC excitation signal, typically between 1–10 mVpp [8] [7]. At higher amplitudes, the response deviates from ideal sinusoidal form, causing harmonic distortion and invalid measurements. However, making the excitation too small reduces signal-to-noise ratio, so 10 mVpp is commonly used to balance linearity and measurement quality. A key advantage of EIS is the ability to simulate the electrochemical system using equivalent circuit models. These models represent the various resistive, capacitive, and diffusive elements that represent the behaviour of the system [7]. This is due to the frequency domain nature of EIS, in comparison with other techniques such as voltammetry that works in the time-domain, thus allowing the behaviour of distinct processes that dominate at certain frequencies to be characterised [7]. By fitting experimental impedance data to these models, parameters such as charge transfer resistance and double-layer capacitance can be extracted, which correlate with biomolecular interactions

occurring on the electrode surface [5]. This capability makes EIS a powerful tool for label-free biosensing applications.

EIS biosensors can be categorized into two main types based on their transduction mechanism: faradaic and non-faradaic sensors.

2.2.1. Faradaic vs Non-Faradaic EIS Sensors

In faradaic measurements, charge transfers occur at the electrode-solution interface and redox reactions occur on the electrode surface [9]. The basic equivalent circuit model for faradaic sensors is the Randles circuit (Figure 2.1a), consisting of solution resistance (R_s) in series with the parallel combination of double-layer capacitance (C_{dl}) and charge transfer resistance (R_{CT}) plus Warburg impedance (Z_w) representing diffusion processes [9].

Non-faradaic measurements operate without charge-transfer reactions, functioning as capacitive sensors that detect changes in the electrical double layer capacitance. Due to the lack of charge-transfer, R_{CT} becomes infinitely large, thus creating an open circuit [9]. On solid electrodes, the observed impedance response of C_{DL} differs from an ideal capacitor, thus a constant phase element (CPE) is used instead of C_{DL} in the Randles non-fardaic equivalent circuit (Figure 2.1b).

(a) Faradaic Randles Circuit

(b) Non-Faradaic Randles Circuit
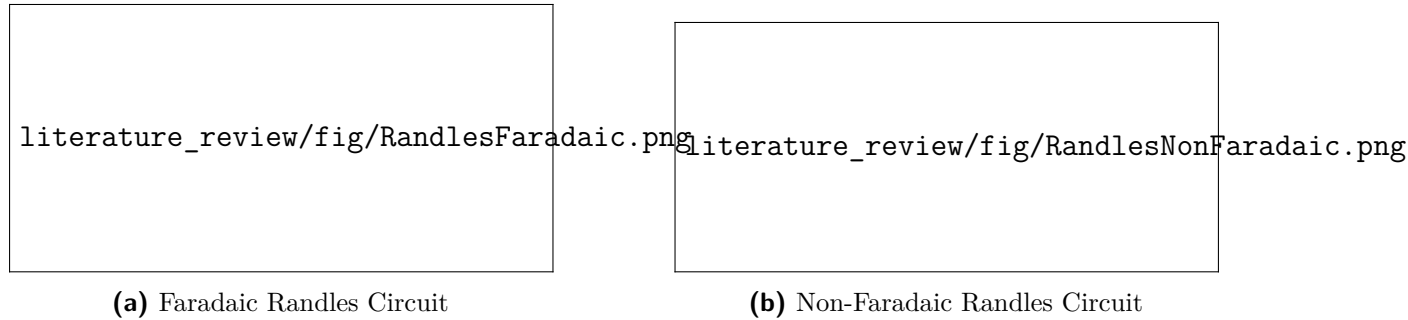
Figure 2.1: Equivalent Circuits for Faradaic and Non-Faradaic EIS Biosensors

EIS produces complex impedance data which contain both magnitude and phase information across a range of frequencies. This data is what allows for the characterisation of the electrochemical system and the extraction of parameters through equivalent circuit modelling.

2.3. Complex Impedance

The complex impedance can be calculated as:

$$Z(\omega) = \frac{V(\omega)}{I(\omega)} = Z'(\omega) + jZ''(\omega) \tag{2.1}$$

where $Z'(\omega)$ is the real component representing resistive behaviour and $Z''(\omega)$ is the imaginary component representing capacitive or inductive behaviour (with $V(\omega)$ and $I(\omega)$ representing the phasor voltage and current respectively) [7].

Two major ways of visualizing this complex impedance are the Nyquist and Bode representations, each highlighting different aspects of the electrochemical response.

2.3.1. Nyquist Plot

A Nyquist plot displays the negative imaginary part of impedance($Z''(\omega)$) versus the real part ($Z'(\omega)$) [10]. Each point on the plot corresponds to a particular frequency, though the frequency is not explicitly shown along the axes. For biosensing, high-frequency data points are located near the origin (low impedance), while low-frequency points are farther along the curve (high impedance). The Nyquist plot has the distinct advantage that some circuit parameters can be read directly form the plot [10].

A purely resistive impedance is represented as a point on the x-axis, as it has no imaginary component and is not frequency dependent. A purely capacitive impedance on the other hand is represented as a straight vertical line on the y-axis, as it has no real component and its imaginary component varies inversely with frequency [10]. The series combination of resistive and capacitive elements, thus result in a vertical line, offset from the y-axis. The parallel combination of resistive and capacitive elements, however result in a semicircular arc, as current flows though the path of least resistance [10]. At low frequencies, the capacitor acts as an open circuit resulting in the x-axis intercept (or diameter of the semi-circle) representing the magnitude of the resistive elements in the circuit. The series combination of a resistor and parallel resistor-capacitor thus results in a semicircular arc offset from the y-axis.

For simple electrochemical systems such as a Randles cell, the Nyquist plot appears as a semicircle (frequencies where charge transfer phenomena dominate) ending in a straight line tail (frequencies where mass transfer phenomena dominate) (Figure 2.2) [7]. The series resistance (R_s) can be read directly from the x-axis intercept at high frequencies (closer to the origin), while the charge transfer resistance (R_{CT}) is given by the diameter of the semicircle in middle frequencies. At low frequencies, the Warburg impedance (Z_w) manifests as a 45-degree line due to diffusion-limited processes [7], explaining the observed tail.

The non-faradaic Randles equivalent, however does not exhibit a semi-circle, due to the exclusion of the charge transfer resistance (R_{CT}) and Warburg impedance (Z_w). Instead, the Nyquist plot appears as a straight line with an x-axis intercept representing R_S. For solid electrodes, however the line is not vertical as would be expected from the series combination of a resistive and purely capacitive element [9] (Figure 2.2b). The C_{DL} is thus replaced with a CPE in the circuit model to account for this non-ideal capacitive

behaviour.

(a) Faradaic Randles Circuit [7]

(b) Non-Faradaic Randles Circuit [9]
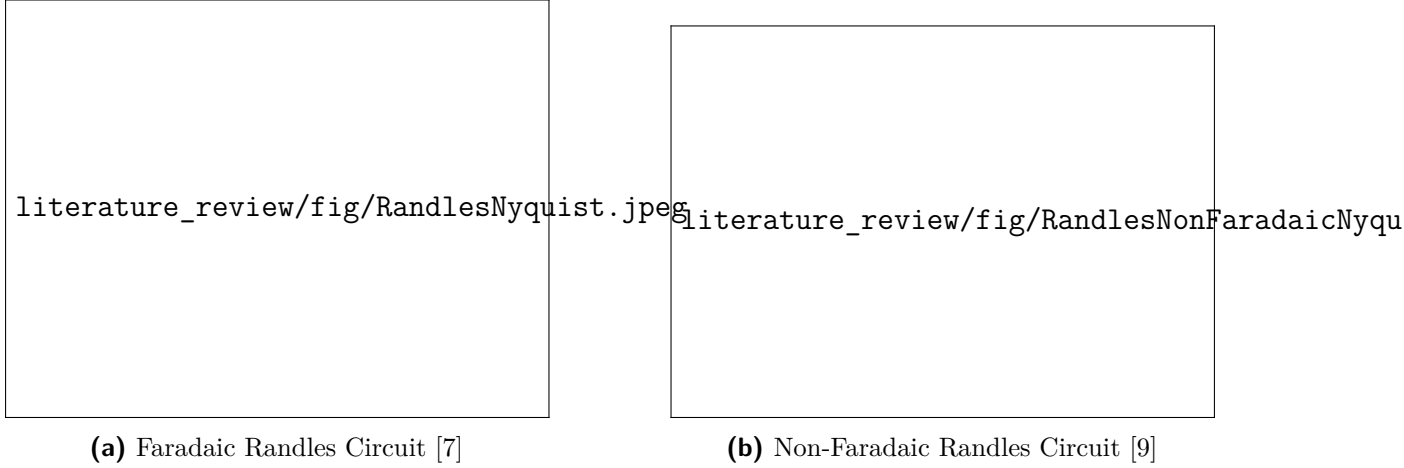
Figure 2.2: Nyquist Plots of Faradaic and Non-Faradaic Randles Circuits

$$Z_{CPE} = \frac{1}{T(j\omega)^\alpha} \tag{2.2}$$

The impedance of the CPE is given by Equation 2.2, with ω representing the angular frequency, T being a constant related to capacitance, and α being an exponent between 0 and 1 that characterizes the deviation from ideal capacitive behaviour [9]. α corresponds to the angle of the line in the Nyquist plot. When $\alpha = 1$, the CPE behaves as an ideal capacitor, while values less than 1 indicate increasing non-ideality due to factors such as surface roughness or inhomogeneities [9].

An alternative representation of complex impedance data is the Bode plot.

2.3.2. Bode Plots

A Bode plot presents the magnitude, $|Z|$, and phase, ϕ, of the impedance as functions of frequency on a logarithmic scale. The Bode magnitude plot reveals how impedance changes with frequency, while the phase plot shows the transition between capacitive ($\phi = -90°$) and resistive ($\phi = 0°$) behaviour. While Nyquist plots offer direct visualization of resistive and capacitive interactions, Bode plots highlight the frequency dependence and allow clearer distinction of time constants [10]. In EIS analysis, both representations are complementary: Nyquist plots assist model-based fitting, whereas Bode plots verify consistency and highlight transition frequencies.

To obtain impedance measurements, specialised instrumentation known as impedance analysers are employed.

2.4. Impedance Analysers

Impedance analysers integrate signal generation, voltage and current measurement, and data processing to determine the complex impedance of a DUT. In biosensing, these devices perform EIS by applying a known AC excitation and measuring the resulting voltage and current responses over a range of frequencies. The ratio of these phasor quantities provides the frequency-dependent impedance, revealing biochemical interactions at the electrode–electrolyte interface [7].

Commercial solutions such as the PalmSens4, Gamry Reference 600+, and Metrohm Autolab PGSTAT offer exceptional accuracy, broad frequency ranges (typically 10 μHz to 1 MHz or higher), and advanced analytics including integrated equivalent circuit fitting [11]. However, these instruments are prohibitively expensive ($\approx$ €4200 for the PalmSens4) and require significant technical expertise to interpret results. This makes them unsuitable for low-resource POC settings where portability, cost, and ease of use are crucial [4]. Miniaturised, low-cost impedance analysers are therefore being actively developed for POC applications [4, 12–14]. Such designs prioritise simplicity, automation, and affordability, while maintaining sufficient frequency range and measurement accuracy to detect biological binding events.

The analogue frontend of an impedance analyser typically consists of three main subsystems: signal generation, voltage measurement, and current measurement.

2.4.1. Signal Generation

EIS requires the generation of a small AC excitation signal, either voltage or current, to probe the DUT [15]. Generating a small current signal is difficult to do accurately and requires circuits such as the improved Howland current pump [16]. On the other hand, generating voltage signals are simple, and thus the method commonly used in EIS systems [15].

Voltage-based signal generation can use dedicated chips like the AD5933 or custom solutions using microcontroller-based digital-to-analogue converters (DACs). The AD5933 offers integrated frequency sweeps and impedance measurement, making it attractive for simple implementations [17]. However, it has several critical drawbacks. The chip has a DC offset between excitation and measurement stages, which is problematic because biosensing requires bipolar signals with no DC component [18]. DC bias causes charge accumulation at the electrode–electrolyte interface, establishing a net electrochemical potential that drives unwanted redox reactions. Over time, these parasitic reactions alter the interfacial chemistry and change the electrode's impedance characteristics, obscuring the properties that non-faradaic EIS aims to measure. The AD5933 also lacks direct voltage measurement capability and has a minimum measurable impedance of 1 kΩ, further

limiting its suitability for biosensing applications.

In contrast, a DAC and analogue-to-digital converter (ADC) solution implemented on a microcontroller allows precise control of excitation signals, flexible signal processing, and easier integration with multiplexing subsystems.

When generating sinusoidal signals using a DAC, the output is not a smooth analogue waveform but rather a series of discrete voltage steps. These steps introduce high-frequency components and harmonics not present in the original signal. Without filtering, they may interfere with downstream circuitry or cause aliasing during analog-to-digital conversion. An anti-aliasing filter (AA filter), typically a low-pass filter (LPF), is placed after the DAC output to remove high-frequency content and smooth the signal.

The dynamic range of a DAC, expressed in decibels, determines the smallest signal it can produce above its noise floor and is given by:

$$\text{Dynamic Range} = 6.02n + 1.76 \tag{2.3}$$

where n is the number of bits of resolution [19]. The AA filter must attenuate high-frequency components sufficiently so that aliased content falls below this noise floor, whilst maintaining a flat passband response to avoid distorting the intended output's amplitude or phase.

For systems generating signals across wide frequency ranges, a fixed-frequency AA filter becomes unsuitable. A single cutoff frequency cannot accommodate both low and high signal frequencies without either excessive attenuation or inadequate filtering. Variable AA filters address this by allowing dynamic cutoff adjustment. Many require changing resistor values to set the cutoff frequency, which is impractical for rapid frequency changes. Clock-tunable filters, which adjust their cutoff based on an external clock signal, thus offer a more flexible solution for wide frequency sweeps.

While some impedance analyser designs infer the applied voltage by using the known characteristics of the excitation stage [12], this fails to account for parasitic resistances, stray capacitance, drift, and environmental changes. Direct measurement captures all these variations, leading to reliable impedance calculations. This is vital in low-voltage biosensing where small changes significantly affect calculated impedance.

2.4.2. Voltage Measurement

Two common circuits for differential voltage measurements are differential op-amps and instrumentation amplifiers. Differential op-amps are simple and cost-effective but are susceptible to common-mode noise and offset errors [20]. They also have relatively low input impedance, which loads the signal source and affects measurements [20]. Instrumentation amplifiers are specifically designed for high-precision differential measurement. They provide superior common-mode rejection, high input impedance, and excellent accuracy

even with small signals in noisy environments [21]. This is due to their three op-amp design, making them particularly suitable for biosensing where signals can be very small and minimising interference is critical.

Amplifying the measured voltage to fully utilise the ADC's linear range enhances both sensitivity and resolution. By maximising the voltage swing within the ADC's input range, the system can discriminate smaller changes in sensor response, allowing for better detection of low-concentration analytes. However, amplification introduces trade-offs related to gain-bandwidth product, which limits usable bandwidth at higher gains. Multi-stage amplification distributes gain across several stages, allowing higher overall gain whilst maintaining adequate bandwidth across the measurement frequency range.

While the measured voltage is relatively constant, the current through the DUT can vary dramatically depending on its impedance. Thus, accurate current measurement is essential for determining the impedance of the DUT.

2.4.3. Current Measurement

Two primary approaches to measuring current exist, namely shunt resistor based measurement and transimpedance amplifier based measurement.

The most basic method places a small known precision resistor (shunt resistor) in series with the current path and measures the voltage drop across it. Ohm's Law then gives the current. This approach is cheap and easy to implement but has severe drawbacks. The voltage drop across the resistor directly reduces the magnitude of the applied perturbation to the DUT, impacting measurements. For biosensing, where signal levels are already low, even small drops significantly affect sensitivity.

A transimpedance amplifier (TIA) on the other hand, converts input current to a proportional output voltage without introducing significant voltage drop across the DUT. The TIA makes use of the following properties of op-amps:

$$V_n \approx V_p \tag{2.4}$$

$$I_n \approx I_p \approx 0 \tag{2.5}$$

where V_n and V_p are the voltages at the inverting and non-inverting inputs respectively, and I_n and I_p are the input bias currents. The positive input (connected to the DUT) is driven to the same potential as the negative input (ground or reference voltage), thereby ensuring a low-impedance path for the current. Conversely, Equation 2.5 ensures that the TIA has a high input-impedance and that the current from the sensor flows entirely

through the feedback resistor. The output voltage is then given by:

$$V_{out} = I_{in} \times R_{feedback} \tag{2.6}$$

The TIA has the advantage that unlike a shunt resistor, the feedback resistor can be large without affecting the applied signal.

In biosensing with fixed voltage perturbation, current varies dramatically depending on the DUT's impedance; from nanoamperes at high impedance to milliamperes at low impedance. A fixed-gain amplifier is impractical across this dynamic range. It would either saturate at high currents or provide insufficient resolution at low currents. Variable gain amplification, achieved through switchable feedback resistors in the TIA or programmable gain amplifiers (PGAs) in subsequent stages, allows the system to adapt to current magnitude. This ensures output voltage remains within the optimal range for the ADC whilst maximising measurement resolution.

Add linking sentence

2.5. Related Works

Chapter 3

Design and Simulation

This chapter details the development of the BioPal impedance analyzer, progressing from user-centered design principles through circuit design, simulation, and firmware implementation. The design process was guided by understanding POC requirements and translating them into concrete technical specifications.

3.1. Design Philosophy

The design followed Brown's design thinking approach [22], emphasizing user empathy and iterative prototyping. Considering the needs of POC healthcare workers revealed that existing solutions, whether commercial instruments like the PalmSens4 or academic prototypes [12] [13], share a critical limitation: they require users to interpret raw impedance spectra and understand EIS principles.

These insights shaped the project objectives around three core pillars: accessibility, affordability, and multiplexing and directly informed the functional architecture and component selection detailed in the following sections.

3.2. Functional Design Overview

The system can be broken up into multiple subsystems, each fulfilling a specific function in order to create a complete device that meets the requirements. On the most basic level the device consists of the DUTs, an impedance analyser and a user interface. The DUT is the IDE that interacts with the analyte and whose impedance characteristics change based on the analyte concentration. A multiplexer is used to interface between multiple DUTs and the impedance analyser. The impedance analyser can be further broken down into the power supply, excitation stage, voltage and current measurement stages and finally the processing that uses an STM32. The user interface is based on an ESP32 and communicates with the impedance analyser through UART.

design/fig/FullSystemOverview.png

Figure 3.1: System Overview

The system architecture is shown in Figure 3.1. The ESP32 C6 has ADC and DAC peripherals, but their performance is known to be suboptimal for high-precision measurement applications. Furthermore, the lack of direct timer control or direct memory access (DMA) support for these peripherals limits their usability for synchronous signal generation and acquisition. The STM32F303K8 on the other hand is specifically designed for mixed-signal applications, with high-performance ADC and DAC peripherals, advanced timer capabilities and DMA support. However, it lacks support for wireless communication and has limited flash and memory resources, making it unsuitable for complex user interfaces. Thus, a dual-microcontroller architecture was used.

The following sections will first discuss the design of the analogue frontend and then the embedded firmware design.

3.3. Analogue Frontend Design

The analogue frontend is responsible for generating the excitation signal, measuring the voltage across and current through the DUT, and conditioning these signals for digitization by the ADC on the STM32F303K8. The design of each stage is driven by the requirements of accurate impedance measurement across a wide frequency range (1 Hz to 100 kHz) and dynamic impedance range (from $100\,\text{k}\Omega$ to $10\,\Omega$). Each stage is discussed in detail below,

including component selection, circuit design and theoretical performance analysis.

3.3.1. Excitation Stage

The easiest way of producing a controlled voltage signal is using a DAC. Both dedicated DACs and DACs built into microcontroller units (MCUs) were possible options. However the STM32F303K8 was chosen specifically due to its high-performance 12-bit DAC. Using the internal DAC simplifies the design by reducing component count and cost.

The LTC1069 was chosen as the AA-filtering integrated circuit (IC), responsible for removing aliased high frequency components from the DAC output. It provides an 8th order lowpass filter that approximates a raised cosine response (with $\beta = 1$). It has a cutoff frequency of up to 120 kHz (200 kHz when using ± 5 V supply rails) set by an external clock and a linear phase response [23]. The clock-tunable nature is ideal for this project, allowing easy adjustments through a timer on the STM.

$$A_v = \frac{V_{out}}{V_{in}} = -\frac{R_f}{R_{in}} \tag{3.1}$$

To maximise voltage resolution and minimise noise, the full linear range of the DAC is utilised when generating the signal. This requires that the DAC output signal is attenuated from 3 Vpp to the desired 10 mVpp using an inverting op-amp gain stage. From Equation 3.1, $R_f = 1 \ k\Omega$ and $R_{in} = 300 \ k\Omega$ were calculated as suitable values.

Figure 3.2: Complete Excitation Stage Circuit

The expected voltage levels across the DUT are thus too small to be measured directly by the ADC and a voltage measurement stage is required to amplify the signal to fully utilise the linear range of the ADC. This is discussed in the following section.

3.3.2. Voltage Measurement

The STM32F303K8's ADC has a theoretical range of 0-3.3 V, however non-linearities and noise near the rails reduce the effective usable range. A gain of 300 V/V was thus chosen for the measurement stage to amplify the signal from 10 mVpp to 3 Vpp (0.1 V - 3.1 V). Gain-bandwidth product (GBW) represents the -3 dB bandwidth of an op-amp at unity gain. The -3 dB bandwidth of the op-amp can be calculated for a specific gain using Equation 3.2, where A_{noise} represents the noise gain calculated in Equation 3.3 and accounts for non-ideal feedback effects and circuit imperfections [24]. This determines the magnitude and phase response of the amplifier at different frequencies, with higher gains resulting in lower bandwidths and thus more significant gain reductions and phase shifts.

$$f_c = \frac{GBW}{A_{noise}} \tag{3.2}$$

$$A_{noise} = 1 + \frac{R_f}{R_{in}} \tag{3.3}$$

Thus, amplifying the signal by a large factor in a single stage would introduce significant phase shifts and gain reductions at higher frequencies. To mitigate this, a two-stage amplification approach is employed.

The INA331 instrumentation amplifier was selected for the first stage of voltage measurement due to its combination of low offset voltage, high common-mode rejection and low input bias current. The INA331 features a small typical offset voltage of 250 µV, which represents the inherent DC error between the input terminals when no differential signal is applied. It adds directly to the measured voltage, creating a systematic DC error. This DC component is filtered out when processing the fast Fourier transform (FFT), however if it is too large it could cause clipping. The low input bias current of 0.5 pA avoids loading the DUT and influencing current measurements.

The device provides an internal gain of 5 V/V, configurable to higher gains through external resistors according to the relationship $G = 5 + 5 \times \frac{R_2}{R_1}$. Choosing $R_1 = 1\ k\Omega$ and $R_2 = 2\ k\Omega$ results in a gain of 15 V/V. The bandwidth at this gain can be estimated from the datasheet to be 2.3 MHz (as seen in Figure **??** in Appendix **??**). Using equations 3.4 and 3.5, the gain reduction and phase shift at 100 kHz can be estimated as -0.004 dB and -2.49° respectively. While this still needs to be accounted for during calibration, it represents a very flat and linear response leading to a more accurate system.

$$|H(j\omega)|_{dB} = 20 \log \frac{1}{\sqrt{1 + \frac{\omega^2}{w_0^2}}} \tag{3.4}$$

$$\varphi(\omega) = -\tan^{-1}(\frac{\omega}{\omega_0}) \tag{3.5}$$

The second stage uses a TLV9061 op-amp in an inverting gain configuration. With a GBW of 10 MHz and gain of $A_v = -20$ ($A_{noise} = 21$), the expected bandwidth for the TLV gain stage is 476.2 kHz (Equation 3.2). From equations 3.4 and 3.5, an expected -0.094 dB gain reduction and -11.86° phase shift is calculated at 100 kHz.

design/fig/VMeasSchem.png

Figure 3.3: Complete Voltage Measurement Stage Circuit

As mentioned in the following section, the current measurement stage also includes an identical final TLV9061 gain stage. This ensures that any gain reductions and phase shifts introduced by this final stage cancel out during impedance calculation.

3.3.3. Current Measurement

The current measurement stage represents the most complex and arguably most important aspect of the analogue frontend. Accurate current measurement across a wide dynamic range is essential for reliable impedance determination, thus significant effort was spent on the design of this stage.

The architecture consists of three stages: a TIA provides the initial current-to-voltage conversion, followed by a PGA, then a final inverting gain op-amp stage identical to that used in the voltage measurement stage.

Based on measurements of the IDE using the PalmSens4, the expected impedance ranges from $100\,\text{k}\Omega$ at 1 Hz to $10\,\Omega$ at 100 kHz, corresponding to a current range spanning four orders of magnitude (100 nA to 1 mA for a 10mVpp excitaion). This wide dynamic range drives several critical design requirements.

A fixed-gain amplifier is impractical across this range. High gain would saturate at high currents, whilst low gain would not utilise the full ADC range at low currents. Programmable gain is therefore essential. This is achieved through two mechanisms: switchable feedback resistors in the TIA and variable gain in the PGA stage.

The PGA113 offers gains ranging from 1-200 V/V with a high GBW of 10 MHz and is controlled via SPI. It has a low gain error of $\leq 0.3\%$ and extremely low noise at $12\,\text{nV}/\sqrt{\text{Hz}}$. Combined with the final TLV9061 gain stage (identical to the final voltage measurement stage), this provides variable gain from 20 V/V - 4000 V/V after the TIA.

Multiple feedback resistor paths on the TIA enable finer gain segmentation across the input current range, improving measurement precision. The larger feedback resistor handles low currents with maximum resolution, whilst the smaller resistor prevents saturation at high currents.

The OPA3S328 is specifically designed for TIA applications, with a wide GBW of 40 MHz, 0.2 pA input bias and typical input voltage offset of 10 µV. Importantly, it has integrated switches for switching between feedback resistors. However, the switch on-resistance is non-negligible at 90-125 Ω and varies with temperature. This produces gain errors and distortion on the TIA output. This can be addressed by using the second switch and op-amp integrated into the OPA3S328 package to build a buffered multiplexer. An example of this circuit is shown in Figure **??**. The switch senses the TIA output directly at the feedback resistor for each gain, whilst the second op-amp acts as a buffer. The low input bias current of the op-amp ensures negligible voltage drop (a worst case of 1.25 nV), providing an accurate Kelvin sense connection.

To maximise the ADC's range even at the smallest current, the larger feedback resistor is designed to deliver 3 Vpp at the maximum PGA gain. From equations 3.6–3.8, this results in 7.5 kΩ.

$$V_{TIA} = \frac{3}{4000} = 750 \ \mu V \tag{3.6}$$

$$A_{TIA} = \frac{750 \ \mu V}{100 \ nA} = 7500 \ V/A \tag{3.7}$$

$$\therefore R_{f1} = 7.5 \ k\Omega \tag{3.8}$$

The smaller feedback resistor is chosen to give the same overall gain at the maximum PGA gain as the larger resistor gives at the minimum PGA gain. This ensures smooth transitions between gain settings without gaps where currents would be too large for one resistor but too small for the other. The smaller feedback resistor is calculated to be 200 times smaller at $R_{f2} = 37.5 \ \Omega$. This ensures that the ranges from 50 nA - 20 µA and 20 µA - 4 mA are covered respectively, whilst ensuring that the ADC input stays between 1.5 Vpp and 3 Vpp.

In traditional TIA designs a capacitor is placed in parallel with the feedback resistor to provide sufficient phase margin and ensure stability [25]. These designs are, however intended for use with a photodiode, rather than EIS. There are few sources available that discuss the design of a TIA for EIS purposes, where capacitance is what is measured rather than compensated for. These sources do not discuss the necessity of feedback capacitors, thus this has to be derived from theory.

The amount of the output that is fed back to the input of an op-amp is defined as the feedback factor (β) and described by Equation 3.9. Where V_{fb} is the voltage present at the inverting input of the op-amp and V_{out} the voltage at the output. This negative

feedback results in the closed loop gain (Equation 3.10) where the loop-gain refers to $A_{OL} \times \beta$ (Equation 3.11).

$$\text{Feedback Factor} = \beta = \frac{V_{fb}}{V_{out}} \tag{3.9}$$

$$\text{Closed Loop Gain} = A_{CL} = \frac{A_{OL}}{1 + A_{OL}\beta} \tag{3.10}$$

$$\text{Loop Gain} = A_{OL}\beta \tag{3.11}$$

$$\text{PM} = 180° + \varphi_{A_{OL}\beta} \qquad \text{at } |A_{OL}\beta| = 0dB \tag{3.12}$$

When $A_{OL}\beta = -1$ the system becomes unstable. This happens when V_{fb} leads or lags V_{out} by 180°. The phase margin (PM) is thus defined as in Equation 3.12 and describes how close the system is to a 180° phase shift and instability when the loop gain magnitude is at 0dB or 1 V/V (the critical point or f_c). To ensure stability, the PM should be at least 45°, with higher values providing more stability at the cost of transient response [25].

$$C_i = C_j + C_{in} \tag{3.13}$$

$$\beta(j\omega) = \frac{X_{c_i}}{R_f + X_{C_i}} = \frac{1}{1 + j\omega R_f C_i} \tag{3.14}$$

The simplified equivalent circuit of a photodiode TIA circuit has the photodiode junction capacitance (C_J) in parallel with the input capacitance of the op-amp (C_{in}) (see Figures **??** and **??** in Appendix **??**). The feedback factor can be calculated as seen in Equation 3.14. The pole in $\beta(j\omega)$, caused by the combined input capacitance, causes the magnitude of $\beta(j\omega)$ to decrease at a rate of -20dB/decade after the corner frequency (determined by the value of C_i) and the phase to decrease from 0° to -90°. The result is a very small phase margin at the critical frequency and instability (as seen in Figure 3.5). The feedback capacitor in parallel with R_f solves this by adding a zero to $\beta(j\omega)$, cancelling out the pole and thus adding phase margin.

However, the equivalent Randles circuit model of a biosensor differs fundamentally from the model of a photodiode due to the series resistance R_s. The input impedance and feedback factor for the Randles non-faradaic equivalent circuit can be calculated as:

Figure 3.4: Randles Equivalent TIA Circuit with CPE

$$Z_{CPE} = \frac{1}{T(j\omega)^\alpha} \tag{3.15}$$

$$Z_{in} = (R_S + Z_{CPE})||X_{C_{in}} \tag{3.16}$$

$$\beta(j\omega) = \frac{Z_{in}}{R_f + Z_{in}} \tag{3.17}$$

$$\tag{3.18}$$

The circuit parameters of the IDE were calculated using circuit fitting in the PSTrace software that accompanies the PalmSens (see Table 3.1) and values for input capacitance, open loop gain and gain bandwidth were read from the OPA3S328 datasheet. A MatLab script was then used to calculate the loop gain of the system. The response of a Randles equivalent non-fardaic circuit with constant C_{dl} instead of a CPE and the equivalent photodiode model were also plotted. The resulting loop-gain responses are shown in Figure 3.5 and Table 3.2 lists the calculated critical frequencies and phase margins.

Table 3.1: Circuit Parameters

Parameter	Value
CPE Randles Circuit	
R_S	$8.975\,\Omega$
T	6.993×10^{-6}
α	0.785
C_{in}	$4.0\,\text{pF}$
Constant C Randles Circuit	
R_S	$12.3\,\Omega$
C_{DL}	$1436.0\,\text{nF}$
C_{in}	$4.0\,\text{pF}$
Photodiode Equivalent	
C_i	$1436.0\,\text{nF}$

Table 3.2: Stability Analysis Results
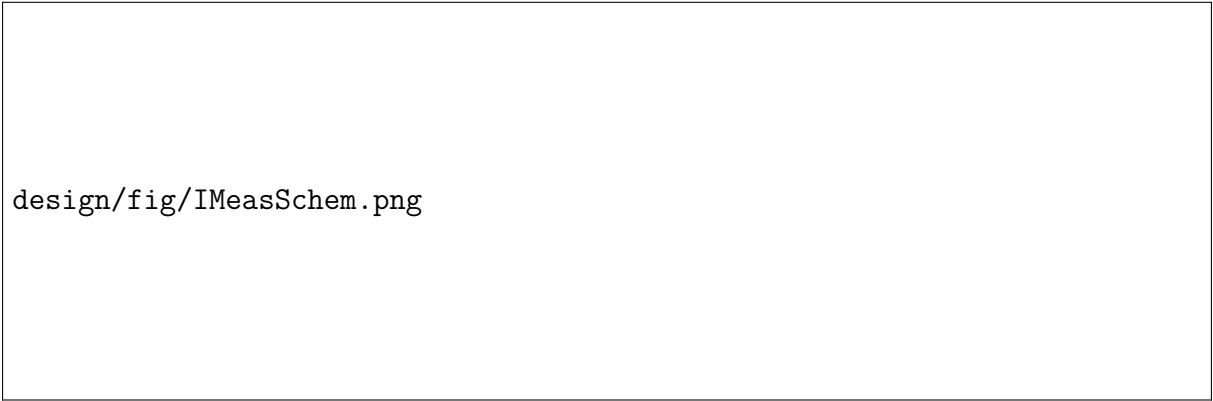
Configuration	f_c (kHz)	PM (°)	Status
$R_f = 7.5\,\text{k}\Omega$			
Photodiode	24.22	0.1	Unstable
Constant C Randles	65.83	82.2	Stable
CPE Randles	64.22	63.8	Stable
$R_f = 37.5\,\Omega$			
Photodiode	343.77	0.5	Unstable
Constant C Randles	9840.03	89.8	Stable
CPE Randles	7725.81	86.3	Stable

design/fig/MatLabLG_7500.png
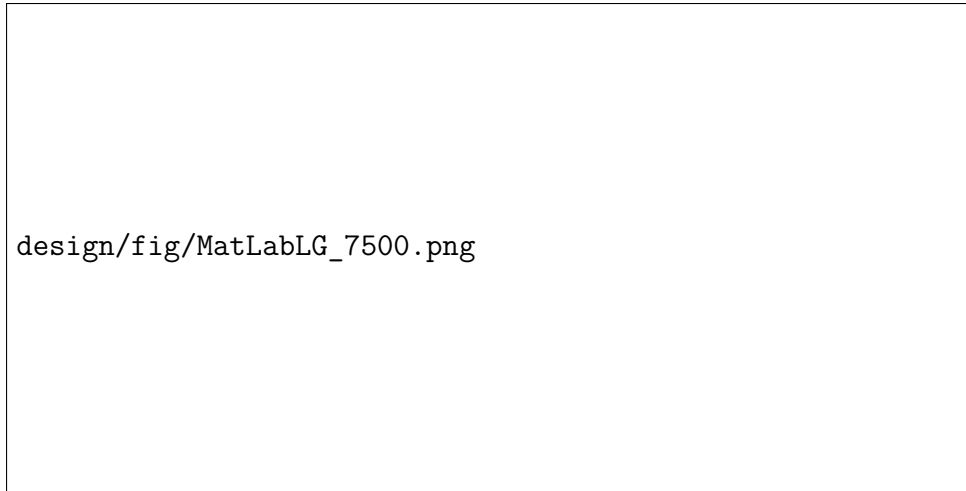
Figure 3.5: Loop Gain Frequency Response for $R_F = 7.5\ k\Omega$

At low frequencies the IDE circuit closely follows the response of the photodiode. This is due to the zero caused by the capacitance dominating the response ($X_{C_{DL}} >> R_S$). However, at higher frequencies R_S dominates and the responses start to diverge. This confirms that ample phase margin is available at both $R_f = 37.5\ \Omega$ and $R_f = 7.5\ k\Omega$,

meaning that no feedback capacitors are needed. At extremely large values of R_F the phase margin reduces, and the system can become unstable ($R_f > 40 \ k\Omega$ for this circuit). Since adding compensation capacitors reduces the bandwidth of the TIA [25], it is not recommended for biosensing TIA circuits, except in cases of extremely high feedback resistor values.

The final current measurement circuit is shown in Figure 3.6.

design/fig/IMeasSchem.png

Figure 3.6: Complete Current Measurement Stage Circuit

Insert Linking paragraph

3.3.4. Multiplexer and IDE interface

While the design and manufacture of IDEs are outside the scope of this project. The IDEs described in [26] were used for this project. To ensure ease-of-use, a method of interfacing with the biosensors that is simple and reliable needed to be developed. Spring-loaded battery connectors were used as they allow the DUT to be easily slid in and out of the device when combined with a 3d printed housing. Insert 3d model of connectors, dut and 3d print.

In order to allow multiple IDEs to be measured by a single analogue front end, a multiplexing solution was required. Various options for multiplexers were considered including dedicated analogue multiplexers (MUX ICs) and relays. Dedicated analogue multiplexers consist of a collection of analogue switches. They typically use CMOS technology, resulting in compact integration and fast switching speeds. Modern analogue switches are available with very low on-resistance ($< 1 \ \Omega$) and a high degree of flatness [27]. However, leakage currents are inherent to these solid-state devices and can corrupt low-current signals, especially in the nanoampere range [27].

Signal relays, in contrast, use electromechanical contacts to physically open or close signal paths, offering near-zero leakage current and extremely low, stable contact resistance that is independent of signal voltage and temperature. This physical isolation and connection ensures that the measured current accurately reflects the biosensor response.

While relays are slower to switch and larger than solid-state alternatives, their switching speed is more than sufficient for switching between sensors.

Figure 3.7:
Relay Multiplexer Topology for 4 IDEs

Figure 3.8: Relay Driver Circuit for one relay

The TXS2-L2-3V DPDT latching signal relay was chosen due to its small size, low operating current (23.3 mA) and high mechanical lifetime (Minimum 200 000 operations). Utilising the DPDT topology of the relay, they can be configured in a tree pattern, allowing for 4 IDEs to be switched using 3 relays as seen in Figure 3.7.

Despite the low operating current, a driver circuit is still needed to power the relay from a microcontroller's general-purpose input/output (GPIO) pins. This consists of a lowside NPN transistor and a flyback diode to protect against voltage spikes when the coil is switched off. The final circuit can be seen in Figure 3.8

Finally, a power supply system needed to be designed to power the entire system.

3.3.5. Power Supply

To ensure portablility, a battery is required. The most cost-effective approach is to utilise a microcontroller with built-in LiPo charging circuitry instead of a dedicated charging circuit. The Firebeetle 2 ESP32 C6 uses an HM6245 low-dropout regulator (LDO), which can supply up to 1 A. This is sufficient to power the rest of the system, from the 3.3 V supply of the ESP32 dev board.

To avoid establishing a DC bias at the electrode–electrolyte interface, the generated excitation must be centred around a stable reference potential. This is achieved using a buffered virtual ground reference at 1.65 V (3.3 V/2) as the midpoint for all analogue circuitry. This approach ensures no DC bias is applied to the DUT whilst negating the need for negative supply rails. Due to the small amplitude of the excitation signal, it needs to be highly accurate and stable. This was done through the use of a matched resistor array and an op-amp buffer. Using a resistor array ensures that our reference is

the exact midpoint of the supply voltage despite any tolerances in the resistor value, while the op-amp buffers this output to avoid loading the resistor array and causing a voltage drop. Choosing a too large resistor value risks a slightly uneven voltage drop due to the small input bias current of the op-amp buffer, on the other hand, a lower value increases the static current draw and power consumption. 1 $k\Omega$ was chosen as a balance between these trade-offs.
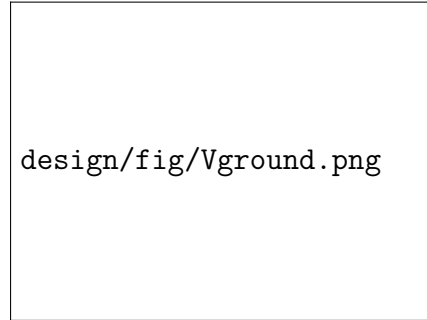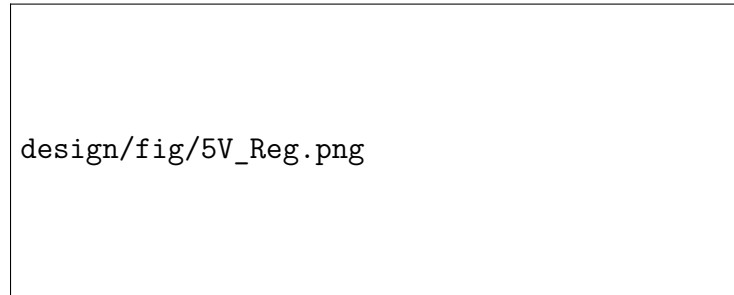

Figure 3.9:
Virtual Ground Reference
Circuit

Figure 3.10: 5 V Boost Converter Circuit

The LTC1069 AA-Filter requires a 5 V supply voltage. A 3.3 V to 5 V boost circuit was thus designed around the TPS61072 boost regulator using the TI WeBench power supply design tool [28], ensuring a stable and efficient circuit as seen in Figure 3.10.

With the complete analogue frontend designed, the next step was to simulate the entire circuit to verify functionality before moving on to PCB design.

3.4. Circuit Simulation

All circuit simulations were performed in LTSpice XVII. The overall system was broken down into subsystems for ease of simulation and verification. Each subsystem was simulated separately before combining them into a full system simulation. All component SPICE models were obtained from the respective manufacturer websites, however for TI products, this required converting PSpice models to LTSpice format.

An accurate model of the IDE is essential for meaningful simulation results and thus was the first step in the simulation process.

3.4.1. IDE

As discussed in Section 2.2.1, CPEs are commonly used to model IDE biosensors due to their non-ideal capacitive behaviour. Despite the widespread use of CPEs in electrical simulations, the SPICE family of simulators lack a native CPE element. The approach described in [29] models a CPE using an array of parallel RC elements. The branches form

a theoretically infinite geometric progression of characteristic frequencies [29], however characteristic frequencies above and below the frequency range of interest are approximated using a single capacitor and resistor respectively. The provided MatLab code was used to calculate the R and C values of all the branches and create a LTSpice model of the CPE based on the paramaters obtained from the PSTrace (Table 3.1). The resulting IDE model closely matches the frequency response obtained from PSTrace (Figure **??** in Appendix **??**). With the model of the IDE confirmed to be accurate, the rest of the system could be simulated.

3.4.2. Excitation Stage

For the simulation of the excitation stage, a sample-and-hold block was used to mimic the DAC at varying sample rates. LTSpice has no included components to simulate a raised cosine filter, thus a FIR filter block from [30] with a raised cosine response and $\beta = 1$ was used. The simulated frequency response compared well with the graphs provided in the LTC1069-7 datasheet (Figures **??** and **??** in Appendix **??**), despite some differences at high levels of attenuation ($< -50dB$). The TLV9061 model and calculated resistor values were used for the simulation of the attenuation stage and the IDE model was connected to complete the excitation stage simulation.

Figure 3.11: Simulated Excitation Stage
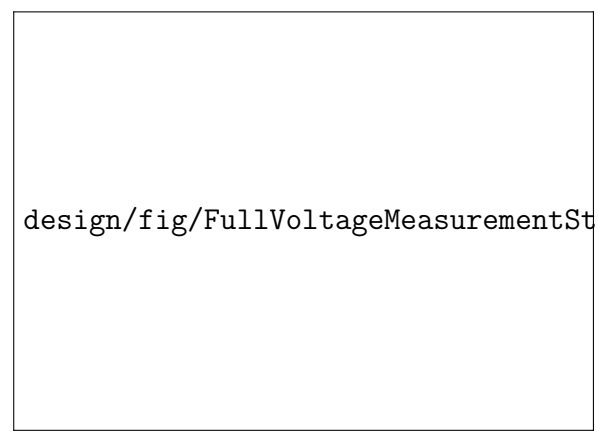
Figure 3.12: Simulated Voltage Measurement Stage

Figure 3.11 shows a 10kHz signal with 32x oversampling generated by the DAC before and after passing through the AA-filter and after being attenuated. The circuit performed as expected and the voltage measurement stage was simulated next.

3.4.3. Voltage Measurement

The voltage measurement stage was simulated with the INA331 and TLV9061 models to confirm the frequency response of the system. The INA331 circuit exhibited only a

slight gain reduction of -0.02dB and a -4.6° phase shift at 100kHz, with the TLV9061 amplification stage contributing an additional -0.2dB gain reduction and -3.4° phase shift. This confirms that sufficient bandwidth is available for measurements up to 100kHz and testing moved on to the current measurement stage.

3.4.4. Current Measurement

The current measurement stage presented the most critical and complex simulation, with the performance and stability of the TIA being key focus areas. Due to problems porting the OPA3s328 PSpice model to LT Spice, the internal mux was not simulated. The PGA113 has no available PSpice model [31], thus a standard inverting amplifier configuration using the TLV9061 was used to simulate the PGA stage. Figure **??** shows the frequency response of the TIA stage alone at both feedback resistor values. At 100 kHz with $R_F = 7.5$ $k\Omega$, the stage exhibits a gain increase of +0.136 dB and a phase shift of -15.4°. For $R_F = 37.5$ Ω, the response shows a gain increase of +0.137 dB and a phase shift of -15.6°. The slight gain increase is due to very slight peaking in the frequency response before the eventual rolloff. This demonstrates a very flat frequency response well below the circuit's bandwidth limitations. Figure 3.13 shows the overall frequency response of the current measurement stage with the PGA and final amplification stages contributing an additional -0.25dB gain reduction and -4.8° phase shift. This confirms that sufficient bandwidth is available for measurements up to 100kHz.

To confirm the stability of the TIA circuit, Tian's method was used to plot the loop gain and phase margin for both the Randles circuit using the CPE and the simplified circuit using a constant capacitance as seen in Figure **??** and Table **??**. These results closely match the MatLab results in section 3.3.3, confirming that the TIA design is stable without the need for feedback compensation.

design/fig/FullCurrentMEasurementStageFreqResponseForRf_37.5.png design/fig/FullCurrentMEasurementStageFreqRespo

(a) $R_F = 37.5$ Ω, PGA Gain = 100 V/V   (b) $R_F = 7.5$ $k\Omega$, PGA Gain = 100 V/V
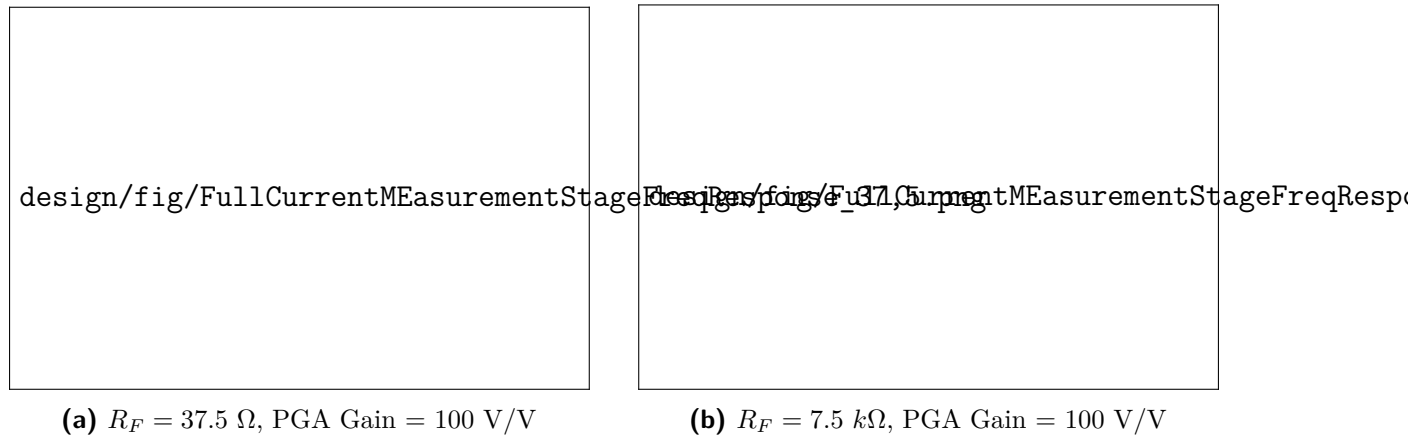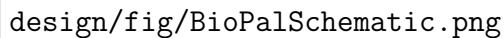
Figure 3.13: Simulated Complete Current Measurement Stage Frequency Response

For testing the complete system, individual subsystems were combined including the DAC and ADCs using sample-and-hold blocks. Transient analysis was done at a range of

excitation frequencies. For frequency analysis the DAC and ADCs were excluded. This confirmed that the subsystems performed similarly to the individual simulations and the PCB could thus be designed around this circuit.

3.5. PCB Design

All PCB design was done using KiCad due to its open-source nature and wide usage in industry. Due to the complexity of the circuit, JLC PCB was used for manufacturing rather than Stellenbosch University's in-house PCB manufacturing. Table **??** in Appendix lists the key limits of JLC's standard PCB process that had to be taken into account.

design/fig/BioPalSchematic.png

Figure 3.14: Complete PCB Schematic

Another key consideration when designing the PCB was minimising noise and interference in the analogue circuitry. Given the limitations of a two-layer PCB, maintaining a continuous and low-impedance ground reference was a key priority, as a fully dedicated ground plane was not practical. To achieve this, both layers incorporated extensive ground copper pours connected through frequent stitching vias to minimise loop inductance and reduce electromagnetic interference (EMI) coupling between layers. A single unified ground network was chosen over separate analogue and digital grounds, as is modern best practice for low-current mixed-signal systems [32]. Instead, the analogue and digital sections were

physically partitioned, with sensitive analogue components and signal routed away from high-speed digital traces. Fencing vias were deployed along region boundaries to confine high-frequency digital currents and provide additional shielding for low-level analogue signals (Figure **??**).

Subsystems we're grouped together with jumpers connecting subsystems, allowing for easier debugging and testing. Care had to be taken in selecting the pin usage for both the STM32 and ESP32 as nearly all pins on both devices were used.
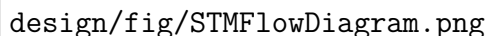
The complete PCB schematic is shown in Appendix **??** and the final PCB layout in Figure **??**.

3.6. Firmware Development

The embedded system architecture was driven by the POC requirements of ease of use without technical expertise, versatility across diverse clinical settings and reliable measurements. To avoid dependence on external software and ensure the device can operate in any environment, all processing is performed on-device.

Figure 3.1 gives an overview of the system architecture. The STM32 serves as the measurement subsystem, interfacing with the analogue frontend to perform measurements. Results are then sent to the ESP32 via UART. The ESP32 acts as the system controller, managing calibration, sending commands to the STM32 and handling the user interfaces. An on-device LCD with buttons provides an interface for standalone operation in any setting, while an optional web-based interface accessible via Bluetooth Low Energy (BLE) enables enhanced usability when client devices are available.

3.6.1. STM32 Measurement Subsystem

```
design/fig/STMFlowDiagram.png
```

Figure 3.15: STM32 Measurement Subsystem Flowdiagram

The STM32F303K8 was selected for its superior measurement capabilities compared to the ESP32. Its 12-bit DAC and 12-bit ADCs provide 1 Msps sampling with hardware oversampling support, whilst advanced timers enable precise frequency generation with sub-microsecond accuracy. The ARM Cortex-M4F core includes a hardware floating point unit (FPU) and digital signal processing (DSP) extensions, providing native support for FFT operations through the CMSIS-DSP library. These capabilities enable the accurate impedance measurements required for biosensing applications.

The 38 measurement frequencies were carefully selected to ensure exact generation by the DAC. Timer frequency generation on the STM32 follows Equation 3.19, where f_{TIM} is the timer clock frequency (64 MHz for TIM6), PSC is the prescaler register value, and ARR is the auto-reload register value. Both PSC and ARR are 16-bit registers with maximum values of 65535.

$$f_{update} = \frac{f_{TIM}}{(PSC + 1) \times (ARR + 1)} \tag{3.19}$$

For a target frequency f_{target}, suitable PSC and ARR values must be found such that $(PSC+1) \times (ARR+1) = f_{TIM}/f_{target}$ and $f_target = f_{meas} \times n_{oversampling}$. This constraint limits the achievable frequencies to those with integer divisors that fit within the 16-bit register limits. The selected frequencies follow roughly logarithmic spacing from 1 Hz to 100 kHz to provide adequate coverage of the biosensor's impedance spectrum.

TIM6 serves dual purposes, triggering both DAC updates for signal generation and ADC sampling for voltage and current measurements. This synchronous triggering is critical for accurate phase measurements, as any timing mismatch between current and voltage measurement would introduce phase errors. Oversampling improves DAC resolution and reduces aliasing effects on the DUT. At low frequencies, 128x oversampling is used (128 DAC updates per sine wave cycle), limited by the maximum ADC buffer size the STM32's 16 KB RAM can accommodate. At higher frequencies, oversampling was reduced due to the limited update speed of the peripherals. However, even at 100 kHz, 32x oversampling is maintained, well above the theoretical Nyquist limit of 2 samples per cycle.

DMA channels enable simultaneous DAC output and dual-channel ADC sampling without CPU intervention. The STM32 controls the PGA gain via SPI, switches the TIA feedback resistor, and manages the relay multiplexer to select between the four DUTs.

Initially, a dynamic gain adjustment approach was implemented where the PGA and TIA gains were automatically adjusted based on measured signal amplitudes to maximise ADC range utilisation without clipping. However, this resulted in large run-to-run variations and proved difficult to calibrate for. Fixed gain settings for each frequency were instead adopted based on the expected impedance response of the biosensor being measured, providing consistent and repeatable measurements.

The measurement process follows a state machine architecture. After receiving a start command from the ESP32 via UART, the STM32 sequences through each frequency for each DUT in turn. For each measurement point, the system first generates the excitation signal and waits 1 second for the response to reach steady state. It then acquires 10 complete cycles of both voltage and current waveforms. These 10 cycles are then averaged to improve the signal-to-noise ratio before FFT processing. A 128-point FFT is performed on both the voltage and current signals using the ARM CMSIS-DSP library, extracting the magnitude and phase at the frequency of interest. After completing all 38 frequencies for a

DUT, the STM32 transmits the results to the ESP32 before proceeding to the next DUT. This immediate transmission after each DUT is necessary due to memory limitations.

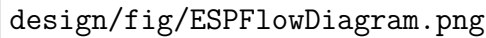## 3.6.2. ESP32 User Interface and System Control

design/fig/ESPFlowDiagram.png

Figure 3.16: ESP Flow Diagram

The ESP32-C6 serves as the system controller, accepting user inputs, sending measurement commands to the STM32, calibrating the resulting measurements and displaying results to the user. The larger flash and RAM resources on the ESP32 allowed for the use of Free RTOS, using three concurrent tasks to handle different aspects of system operation. A UART reader task receives and parses data packets from the STM32 as they arrive. A data processor task performs impedance calculations and applies calibration corrections to the raw measurements. A GUI task manages the display updates, button inputs, and BLE communication. This multi-tasking approach ensures responsive user interaction whilst processing measurement data in real-time.

The ESP32 orchestrates the complete measurement sequence. Upon receiving a start command from either the physical buttons or web interface, it configures the STM32 with the appropriate measurement parameters (number of DUTs and frequency range) and initiates the measurement cycle. As the STM32 send measurement data back via UART, the ESP32 applies calibration corrections and updates the display to show measurement progress. The calibration system corrects for systematic errors in the analogue frontend using reference measurements. After completing measurements for all DUTs, the ESP32 stores the results and makes them available for export via USB serial in a CSV format and sends the data over BLE to the web interface if connected.

On-Device Interface

Physical buttons and a TFT LCD display enables complete standalone operation. Combined with battery power, this ensures the device functions in any resource-constrained setting without requiring external hardware. The high resolution display allows for an intuitive user interface. Users can configure the number of DUTs to measure, set the frequency range, initiate measurements, and view results without any external devices. This interface is critical for resource constrained POC environments where reliable network connectivity or additional hardware might not be available.

Web Interface via BLE

A secondary web-based interface provides enhanced usability when client devices are available. A website was chosen over an app to ensure compatibility with all modern devices, regardless of operating system. This ensures that computers, phone or tablets can all be used to control the device. Three implementation approaches were considered for enabling remote control of the device via a web interface.

design/fig/BioPal WebUI.png

Figure 3.17: Web Interface Results Page

Trim down **Option 1 - Existing WiFi Network:** The device connects to an existing network, enabling control over WiFi or the internet. While convenient once configured, this approach poses significant barriers in healthcare environments with strict network security policies due to the need to protect patient data. It also excludes settings without existing WiFi infrastructure, such as rural clinics.

Option 2 - Device WiFi Hotspot: The device hosts its own WiFi network, serving a local website. This avoids secure network requirements and functions everywhere, but forces client devices offline, potentially disrupting other applications and services.

Option 3 - Web Application with BLE: A web application hosted remotely connects to the device via BLE usin the WebBLE protocol. This approach was selected as it provides the benefits of both previous options without their drawbacks. Client devices maintain internet connectivity, no secure network authentication is required, and the solution works universally. Critically, all measurement data transfers locally over BLE, eliminating security risks and POPIA compliance concerns associated with transmitting patient information over the internet.

After completing all other aspects of hardware and software, the complete system needed to be integrated to ensure a cohesive user experience.

3.7. System Integration

The system was enclosed in a plastic case, with cutouts provided for the LCD, buttons and IDEs connectors. A power button and panel-mount usb c port that supports both charging and data transfer were added. Additionally a near-field communication (NFC) tag and QR code were included on the top of the case to provide easy access to the web interface. The final assembled device can be seen in Figure 3.18.

design/fig/IntegratedSystem.jpg

Figure 3.18: Complete BioPal Device

The device was then validated using lab testing to measure performance against reference equipment.

Chapter 4

Testing & Validation

The testing and validation process was structured to systematically verify the functionality of the impedance analyser, progressing from subsystem verification to complete system integration and finally calibration and validation with IDEs and lab tests.

4.1. PCB Testing Methodology and Results

The assembled PCB was visually inspected, and continuity testing confirmed no obvious short circuits or discontinuities. The ESP32's onboard battery charging circuit and regulator was confirmed to supply a stable 3.3 V rail to all digital and analogue components with enough current to avoid brownouts. The virtual ground reference circuit was measured at exactly 1.650 V. The TPS61072 boost converter successfully provided a stable 5 V supply for the LTC1069 anti-aliasing filter.

Next, each subsystem was tested individually whilst other subsystems remained disconnected. This approach allowed for precise characterisation of each stage's performance and simplified fault diagnosis.

4.1.1. Excitation Stage

The excitation stage was tested using a signal generator providing a 3 Vpp input signal and an oscilloscope to measure the attenuated output. Unfortunately, the LTC1069 anti-aliasing filter was found to be dead-on-arrival. Given the significant lead times for component procurement and project time constraints, it was not feasible to order a replacement. The filter would have improved performance at very low frequencies, but was not a critical part of the system and therefore the excitation stage was tested without it. Whilst this introduces higher-frequency components from the DAC's stairstepping, the synchronisation of DAC generation and ADC sampling and FFT frequency extraction helps to minimise the impact on measurements. The attenuation stage was characterised across the full frequency range from 1 Hz to 100 kHz. The resulting signal was measured at ≈10.33 mVpp, giving a 290 V/V attenuation, with a flat frequency response. This is close to the designed 10 mVpp and well within the ideal range for biosensing applications and our voltage measurement stage.

4.1.2. Voltage Measurement Stage

For the voltage measurement stage, both the INA331 instrumentation amplifier and TLV9061 gain stage were tested separately. The INA331 was tested using a 200mV input signal to minimise noise from the signal generator. It performed as expected, with no measurable gain roll-off at 100 kHz and a phase shift of -5°, which is close to the expected -4.6° based on simulations.

The TLV9061 stage was similairly tested using a 150mV input signal to avoid clipping on the output. It performed well, exhibiting a less than 0.2 dB gain roll-off and -8.7° phase shift at 100 kHz compared to the expected -3.4°. The larger-than-expected phase shift can be attributed to tolerances in the op-amp's gain-bandwidth product.

Overall, the voltage measurement stage's performance closely matched expectations, with the phase offsets remaining well within acceptable limits for accurate impedance measurements if properly calibrated for.

While the applied voltage is roughly known, the current varies significantly based on the impedance. Therefore, the current measurement stage was the most critical to verify.

4.1.3. Current Measurement Stage

The current measurement stage required the most extensive testing due to its complexity and switchable gain configurations.

The TIA was characterised by applying known voltages across resistors of known values, allowing the input current to be calculated. The TIA output voltage was then measured to determine the transimpedance gain across the full frequency range. The resistor values were measured using a standard multimeter (rather than a Kelvin sense connection) and the resistors' parasitic inductance and capacitance were ignored. However, this characterisation served primarily for functional validation, as final calibration would be performed against the PalmSens4.

At $R_f = 37.5\ \Omega$, the TIA exhibited a gain of 37.73 V/V with a phase shift of -4.4° and gain reduction of 0.74 dB at 100 kHz. At the larger feedback resistor value of $R_f = 7.5\ k\Omega$, the gain averaged at 7427 V/V. Interestingly, both phase shift and gain reduction at 100 kHz were less pronounced with the higher feedback value at -3.5° and <0.1 dB respectively. This is possibly due to slight peaking.

Stability was verified by connecting a simplified Randles equivalent circuit with a constant capacitance of 1.47 μF and resistance of 12 Ω, approximating the expected biosensor characteristics (Table 3.1). A 10 mVpp signal was applied to the equivalent circuit and swept from 1 Hz to 30 MHz while monitoring the TIA output for oscillations, ringing, or excessive peaking in the frequency response. No instability was observed, confirming the theoretical analysis in Section 3.3.3.

The PGA113 was measured at each gain setting from 1 V/V to 200 V/V for each

measurement frequency. Table 4.1 summarises the measured gain and phase shift at 100 kHz for each setting. As expected, the phase shift is more pronounced at higher gain settings, however the higher gains will primarily be used at lower frequencies where the phase shift is negligible. These gain and phase shift values were incorporated into the calibration procedure to ensure accurate impedance calculations.

Table 4.1: PGA113 Performance at 100 kHz

Gain Setting (V/V)	Max Gain (V/V)	100kHz Gain (V/V)	Gain Reduction (dB)	100kHz Phase Shift (°)
1	1.00	0.92	-0.74	-0.8
2	2.00	1.84	-0.71	-2.132
5	4.98	4.57	-0.74	-1.634
10	9.97	9.15	-0.74	-2.613
20	21.60	21.52	-0.03	-5.619
50	54.00	53.44	-0.09	-7.491
100	99.92	92.18	-0.70	-14.79
200	198.06	173.17	-1.17	-25.73

As expected, there was no measurable difference in performance between the TLV9061 gain stage in the voltage and current measurement stages. With all subsystems verified individually, the system was integrated and calibrated.

4.2. System Calibration

The complete analogue frontend was tested using passive test cells, initially with a signal generator providing the excitation. Once overall system stability and measurement accuracy were confirmed, the STM32 was used to generate DAC signals and acquire responses with the ADCs.

The STM32's ADC offsets were calibrated using the built-in functions. The gradients were determined by applying a series of known voltages using a bench power supply, with each voltage verified using an oscilloscope and multimeter. Similarly, the DAC output was measured, and the centre point of the generated signal adjusted from 2048 to 2009 to account for the constant voltage offset in the excitation stage attenuation. This ensured that the analogue output was precisely centred at 1.65 V, ensuring the biosensor is not biased with a DC voltage. The DAC's frequency generation capability was verified by measuring the output waveform at each test frequency using an oscilloscope. Frequency response data from each subsystem was smoothed with Locally Estimated Scatterplot Smoothing (LOESS) filtering in MATLAB to minimise measurement noise. The processed data was compiled into a calibration table, stored on the ESP. Finally, a non-faradaic

Randles equivalent test cell (consisting of a 12 Ω resistor and 1.47 μF capacitor in series), was measured with both the BioPal and PalmSens4. This was used to calibrate the BioPal's response against the reference instrument.

It was found that at low frequencies (125 Hz and below), the lack of filtering in the excitation phase, lead to significant aliasing. Due to the DUT's lower impedance at higher frequencies, the aliased high-frequency components dominated the response, leading to clipping at high gain settings or conversely, very low signal levels at the frequency of interest for low gain settings. However, as shown in the following section, these frequencies are below the range of interest for the tested IDEs and thus did not have a significant impact on results. However, it did lead to increased error margins at lower frequencies, especially in phase measurements. Measurements taken with the PalmSens4 taken directly on the test cell and on the output of the multiplexer confirmed that the multiplexer does not influence measurement accuracy.

After calibrating the system, final validation could be done through measurements on IDEs using phosphate buffered saline (PBS) 1x solution and bovine serum albumin (BSA) protein.

4.3. Final Validation Methodology and Results

Initial validation was performed using PBS 1x solutions of varying concentrations to test the BioPal's ability to measure bulk solution impedance changes. Following this, BSA protein binding to the IDEs was used to simulate antibody-antigen interactions, allowing validation of surface-based impedance changes. PBS solutions of v25%, 50% and 75% concentrations were prepared by diluting stock PBS 1x with deionised water with higher PBS concentrations corresponding to higher ionic strength and thus lower solution impedance. Figures 4.1 - 4.3 show impedance measurements taken by both the BioPal and PalmSens4 for each concentration. Baseline measurements were taken using the diluted solutions, followed by final measurements using undiluted PBS 1x. Tabel 4.2 summarises the average reduction in impedance magnitude between the baseline and final measurements across the frequency range from 125 Hz - 100 kHz. This also confirmed the usefulness of the multiplexed system when taking multiple measurements.

Table 4.2: Average Impedance Change from Baseline to PBS 1x (125 Hz - 100 kHz)

PBS Concentration	25%	50%	75%
PalmSens4 Reduction	45.6%	34.2%	12.9%
BioPal Reduction	47.1%	31.7%	12.4%

(a) BioPal

(b) PalmSens4
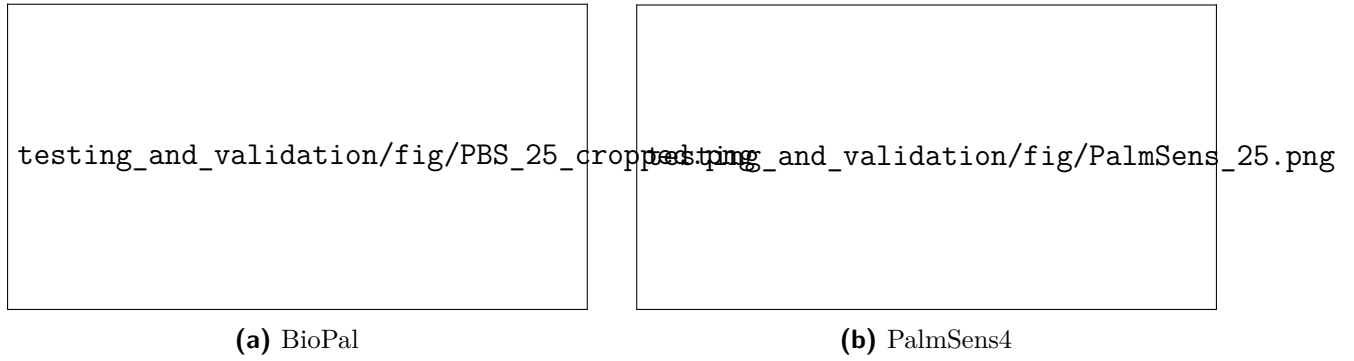
Figure 4.1: 25% Baseline vs 100% Final PBS 1x Comparison

(a) BioPal

(b) PalmSens4
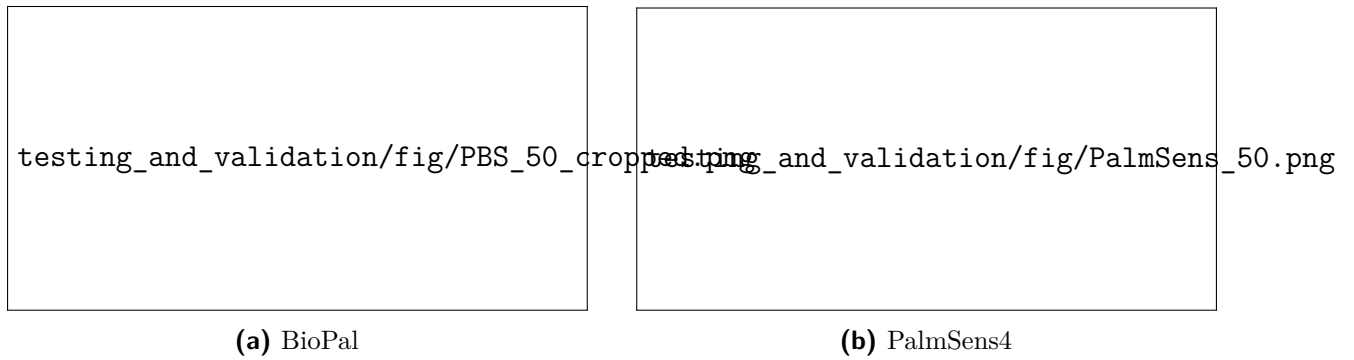
Figure 4.2: 50% Baseline vs 100% Final PBS 1x Comparison

(a) BioPal

(b) PalmSens4
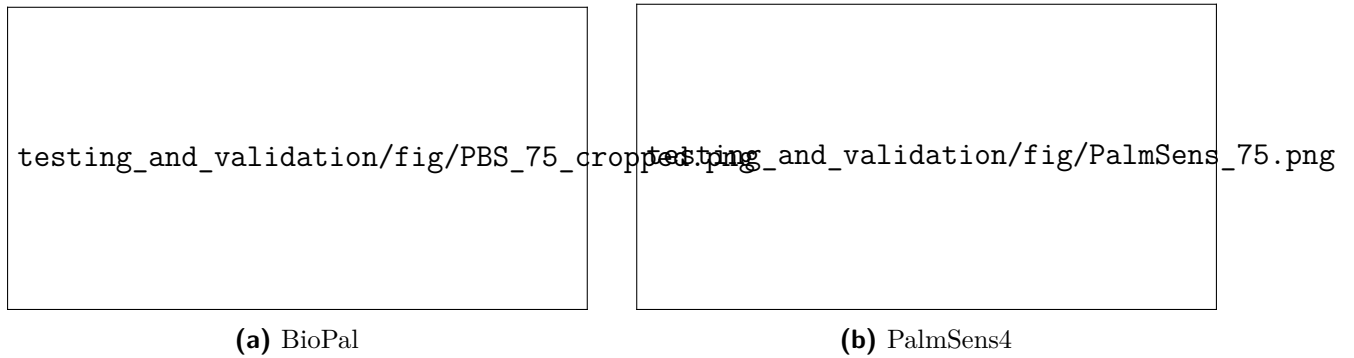
Figure 4.3: 75% Baseline vs 100% Final PBS 1x Comparison

After validating the ability to distinguish bulk solution impedance changes, sensitivity to surface-based impedance changes needed to be confirmed. While testing with immobilised antibodies and actual protein antigens would provide the most direct validation, this was beyond the scope of this project due to laboratory safety restrictions, cost constraints, and limited time. Instead, BSA was used as a surface-binding protein to simulate antibody-antigen interactions. BSA is a common blocking protein that is readily absorbed by gold electrode surfaces, creating a protein layer that alters the interfacial impedance characteristics. This mimics the effect of antibody-antigen binding on the electrode surface.

The measurement methodology involved establishing a baseline impedance measurement in PBS 1x, removing the PBS and adding BSA solution to the electrode well, allowing 20 minutes for protein adsorption, flushing the electrode three times with fresh PBS 1x to remove unbound protein and thus maintaining the same solution characteristics, and finally performing a second impedance measurement.

Existing literature use BSA concentrations ranging from 1 mg/mL to 60 mg/mL for impedance based biosensor sensitivity validation [33] [34]. In this work, three concentrations were selected: 20 mg/mL, 50 mg/mL and 100 mg/mL.

Measurements were performed at each step using both the BioPal and the PalmSens4 for direct comparison. Figures 4.4 - 4.6 shows the impedance magnitude and phase measurements from both instruments before and after BSA binding, showing a clear difference between concentrations. Figures 4.7 - 4.9 show the relative change in magnitude across the frequency range. It was found that the largest impedance changes occurred in the frequency range from 160 Hz to 500 kHz. The average change in this range was used to give a qualitative result. The device gives the user a risk level of disease presence ranging from none to high based on the following thresholds:

Table 4.3: Qualitative Risk Levels Based on Impedance Change

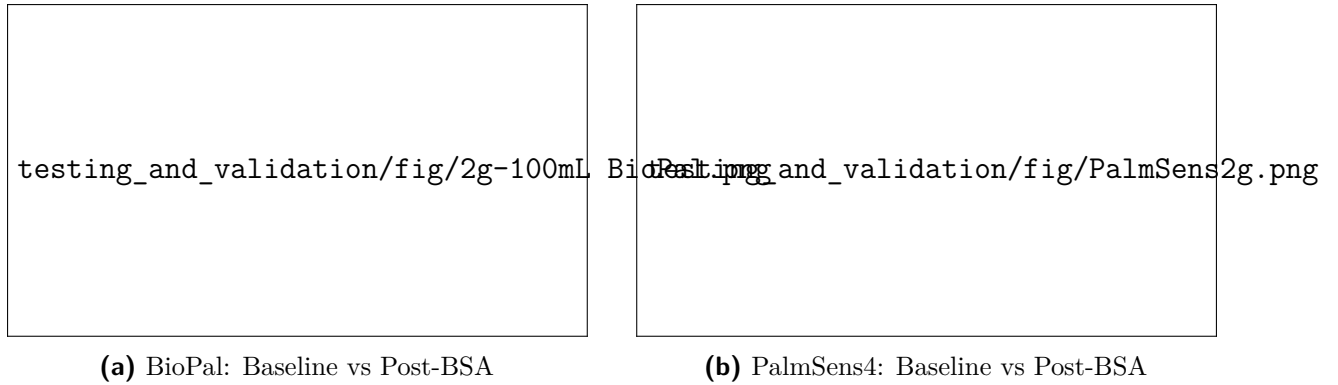| Risk Level	None	Low	Medium	High
Impedance Change	<5%	5% - 15%	15% - 25%	>25%

(a) BioPal: Baseline vs Post-BSA

(b) PalmSens4: Baseline vs Post-BSA

Figure 4.4: Baseline vs Final Frequency Response to 20mg/mL BSA Binding

(a) BioPal: Baseline vs Post-BSA

(b) PalmSens4: Baseline vs Post-BSA
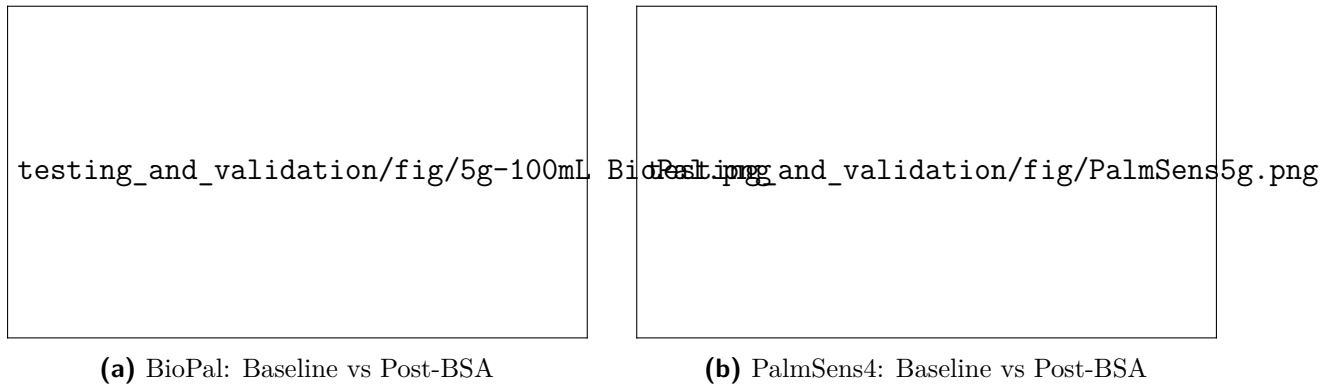
Figure 4.5: Baseline vs Final Frequency Response to 50mg/mL BSA Binding

(a) BioPal: Baseline vs Post-BSA

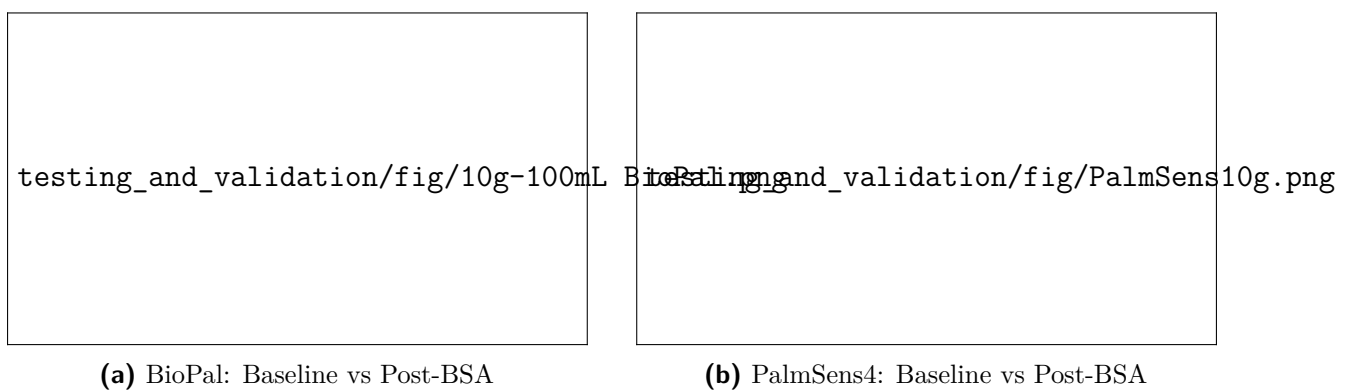**(b)** PalmSens4: Baseline vs Post-BSA

Figure 4.6: Baseline vs Final Frequency Response to 100mg/mL BSA Binding

Table 4.4: Average change in Impedance Magnitude due to BSA Binding (160 Hz - 500 Hz)

BSA Concentration	20 mg/mL	50 mg/mL	100 mg/mL
PalmSens4	2.8%	9.9%	15%
BioPal	6.7%	29.9%	31.7%

(a) Change in Impedance Magnitude

(b) Change in Impedance Phase
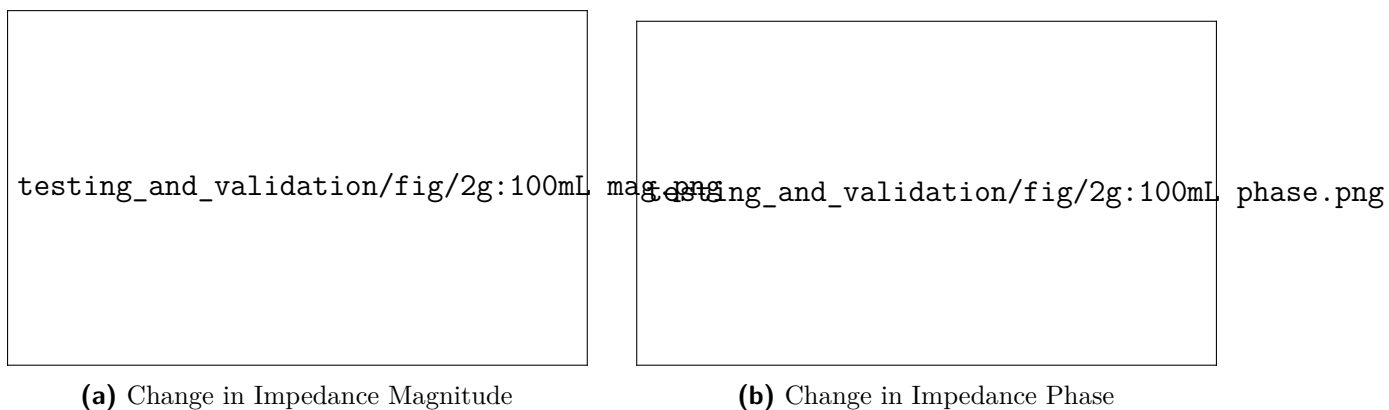
Figure 4.7: IDE Impedance Change with 20 mg/mL BSA Binding

(a) Change in Impedance Magnitude

(b) Change in Impedance Phase
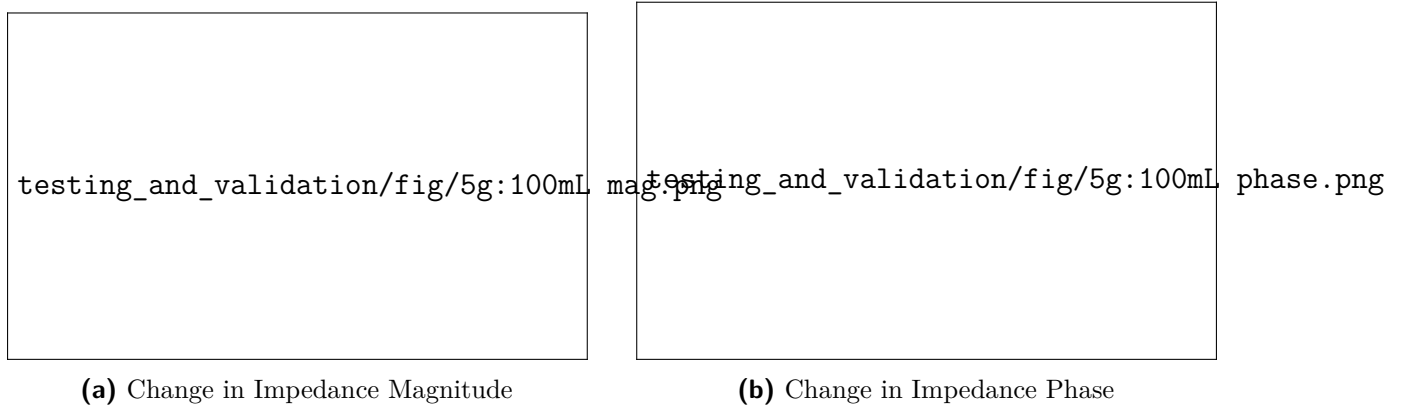
Figure 4.8: IDE Impedance Change with 50 mg/mL BSA Binding

(a) Change in Impedance Magnitude
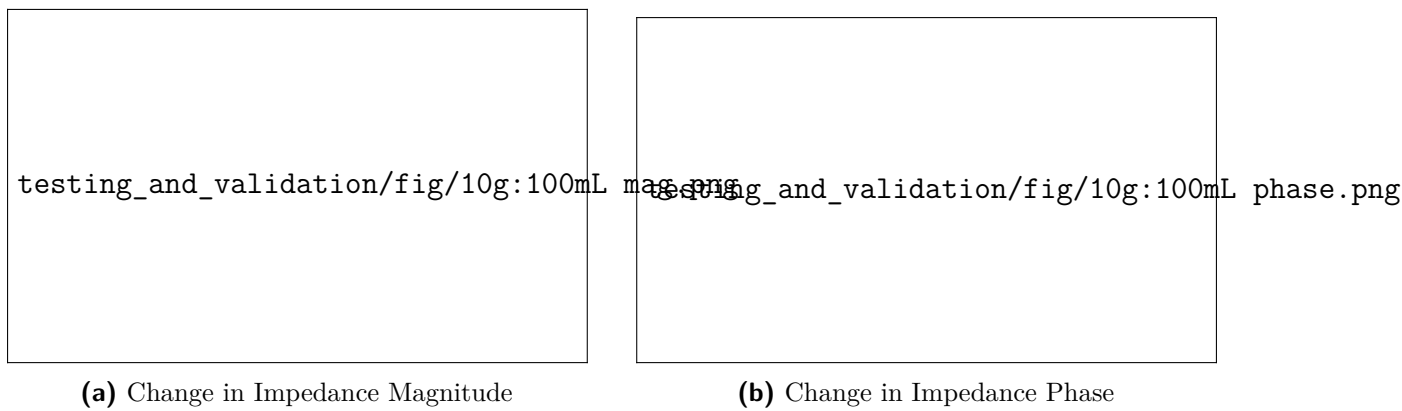

(b) Change in Impedance Phase

Figure 4.9: IDE Impedance Change with 100 mg/mL BSA Binding

4.4. Discussion of Validation Results

The BioPal meets all requirements needed to meet the objectives set out in Chapter 1. All subsystems in the analogue frontend perform close to expectations and well within the requirements. The system is capable of performing impedance measurements with an average run to run standard deviation of 1.03% from 125 Hz to 100 kHz. The majority of run to run variance occurs at lower frequencies due to the lack of anti-aliasing (as seen in Figure **??** in Appendix **??**). The multiplexed measurement system allows for up to 4 IDEs to be measured sequentially without human intervention and without impacting measurement accuracy.

PBS concentration measurements performed exceptionally well, with sub-3% error margins across all tested concentrations (Table 4.2), ensuring that different concentrations can be reliably distinguished. This validates the BioPal's impedance measurement capabilities and the core functionality of the combined system. The lack of AA-filter had an impact at low frequencies, however this did not have an impact on final results due to being outside the range of interest for the tested IDEs. The frequency response closely tracked the

PalmSens4 from 125 Hz to 100 kHz (Figures 4.1 - 4.3), confirming that the calibration procedure successfully compensates for systematic errors in the analogue frontend.

Tests using BSA confirmed that the BioPal can clearly differentiate between different concentrations, albeit with larger error margins against the PalmSens than the PBS tests. Figures 4.7 - 4.9 show that the change in magnitude across the tested frequency range follows a similar pattern between the BioPal and PalmSens. However, the BioPal consistently detected larger changes than the PalmSens. This disparity likely results from the measurement sequence, with baselines first recorded with the BioPal then the PalmSens, while final measurements reversed this order (PalmSens then BioPal). The roughly 10 minute delay between BioPal and PalmSens measurements allowed time-dependent impedance reduction from PBS exposure [35]. Thus, the PalmSens baseline had more time to stabilize and the final had less, while the BioPal baseline had less time to stabilize and the final more time. This emphasises the importance of standardised measurement timing protocols for POC deployment. Despite this, the BioPal was able to reliably distinguish between concentrations, demonstrating its suitability for biosensing applications. The risk level classification based on impedance change (Table 4.4) functioned as intended, providing a straightforward interpretation of results for end-users.

Recommendations for future work as well as a summary of the completed project is discussed in the following chapter.

Chapter 5

Summary and Conclusion

This project documents the development and testing of BioPal, a low-cost multiplexed impedance analyser aimed at point-of-care biosensing applications. The device integrates analogue frontend circuitry with embedded firmware and dual user interfaces to enable EIS measurements on interdigitated electrodes without requiring specialised training or external equipment.

The analogue frontend implements voltage-controlled EIS across 1 Hz to 100 kHz using a 12-bit DAC for excitation, instrumentation amplifier-based voltage measurement, and transimpedance amplifier-based current measurement with programmable gain. A relay-based multiplexer enables sequential measurement of up to four IDEs. The complete system was integrated onto a custom PCB and housed in a battery-powered portable enclosure. Two user interfaces were implemented: an on-device LCD with buttons for standalone operation, and a web-based interface via Bluetooth Low Energy for enhanced usability.

The project achieved its core objectives. The analogue frontend successfully generates excitation signals and measures voltage and current responses across the target frequency range, enabling microcontroller-based EIS measurements (Objective 1). The multiplexer sequentially measures up to four IDEs (Objective 2). A complete PCB integrating all subsystems was designed and manufactured (Objective 3). Firmware implementing signal processing, FFT-based impedance calculation, and calibration correction was developed for both microcontrollers (Objective 4). Dual user interfaces enable standalone operation with qualitative risk assessment (Objective 5). The device operates from battery power with total component costs of approximately R2,000 (A full cost breakdown is shown in Table **??** in Appendix **??**), well below the R4,500 target (Objective 6). Calibration against the PalmSens4 was completed using test cells and IDEs, with validation demonstrating sub-3% error margins for PBS measurements and successful differentiation between varying concentrations of BSA protein binding (Objective 7).

However, several limitations constrain immediate deployment.

5.0.1. Limitations

The inoperable LTC1069 AA filter limits accurate measurements to frequencies above 125 Hz due to aliasing artefacts, though this proved sufficient for the tested IDEs. This would be easy to replace given more time and would lead to even better accuracy and repeatability. The fixed-gain configuration improves stability but reduces flexibility for IDEs with different impedance characteristics. Validation was restricted to passive components, PBS solutions, and BSA protein. Testing with immobilised antibodies and disease biomarkers or clinical samples were outside the scope of this project. Despite these limitations, the BioPal demonstrates core measurement capabilities and a validated platform for further development toward practical POC biosensing applications.

5.0.2. Recommendations for Future Work

Recommendations for future work towards achieving an accessible POC biosensing system based on the BioPal platform inculde:

- Enable gain settings to be configured via the user interface to accommodate IDEs with varying impedance ranges.

- Conduct tests using a variety of IDEs as well as immobilised antibodies and relevant disease biomarkers to evaluate real-world biosensing performance.

- Establish robust standardised measurement protocols to ensure consistent timing across tests.

- Perform user testing with healthcare workers to assess usability and workflow integration in real-world POC settings.

These recommendations would build upon the validated BioPal platform to advance toward a practical, user-friendly impedance analyser deployed in point-of-care settings.

Bibliography

[1] N. Bhalla, P. Jolly, N. Formisano, and P. Estrela, "Introduction to biosensors," *Essays in Biochemistry*, vol. 60, no. 1, pp. 1–1, Jun. 2016.

[2] "Biomarkers | National Institute of Environmental Health Sciences."

[3] H. Chu, C. Liu, J. Liu, J. Yang, Y. Li, and X. Zhang, "Recent advances and challenges of biosensing in point-of-care molecular diagnosis," *Sensors and Actuators. B, Chemical*, vol. 348, p. 130708, Dec. 2021.

[4] M. Parihar, N. W. N., Sahana, R. Biswas, B. Dehury, and N. Mazumder, "Point-of-care biosensors for infectious disease diagnosis: Recent updates and prospects," *RSC Advances*, vol. 15, no. 36, pp. 29 267–29 283.

[5] J. S. Daniels and N. Pourmand, "Label-Free Impedance Biosensors: Opportunities and Challenges," *Electroanalysis*, vol. 19, no. 12, pp. 1239–1257, 2007.

[6] H. S. Magar, R. Y. A. Hassan, and A. Mulchandani, "Electrochemical Impedance Spectroscopy (EIS): Principles, Construction, and Biosensing Applications," *Sensors*, vol. 21, no. 19, p. 6578, Jan. 2021.

[7] A. C. Lazanas and M. I. Prodromidis, "Erratum: Electrochemical Impedance Spectroscopy-A Tutorial (ACS Measurement Science Au (2023) 3:3 (162-193) DOI: 10.1021/acsmeasuresciau.2c00070)," *ACS Measurement Science Au*, vol. 2023, no. 3, pp. 14–14, 2025.

[8] "EIS Quality Indicators and Linearity Correction."

[9] Q.-Z. Xie, M.-W. Lin, E.-W. Hsu, and C.-T. Lin, "Review—Advancements of Nanoscale Structures and Materials in Impedimetric Biosensing Technologies," *ECS Journal of Solid State Science and Technology*, vol. 9, p. 115027, Oct. 2020.

[10] "Bode and Nyquist Plot."

[11] "PalmSens4," https://www.palmsens.com/product/palmsens4/.

[12] L. A. Buscaglia, J. P. Carmo, and O. N. Oliveira, "Simple-Z: A Low-Cost Portable Impedance Analyzer," *IEEE Sensors Journal*, vol. 23, no. 21, pp. 26 067–26 074, Nov. 2023.

[13] A. Al-Ali, A. Elwakil, A. Ahmad, and B. Maundy, "Design of a Portable Low-Cost Impedance Analyzer," *BIODEVICES 2017 - 10th International Conference on Biomedical Electronics and Devices, Proceedings; Part of 10th International Joint Conference on Biomedical Engineering Systems and Technologies, BIOSTEC 2017*, vol. 2, pp. 104–109, Feb. 2017.

[14] M. Ibrahim, "CMOS Transimpedance Amplifier for Biosensor Signal Acquisition."

[15] M. E. Orazem and B. Tribollet, "A tutorial on electrochemical impedance spectroscopy," *ChemTexts*, vol. 6, no. 2, p. 12, Jun. 2020.

[16] ""Improved" Howland current pump circuit," 2020.

[17] "AD5934 test update | Analog Devices," https://www.analog.com/en/resources/app-notes/an-1252.html.

[18] F. Seoane, J. Ferreira, J. J. Sanchéz, and R. Bragós, "An analog front-end enables electrical impedance spectroscopy system on-chip for biomedical applications," *Physiological Measurement*, vol. 29, no. 6, pp. S267–S278, Jun. 2008.

[19] L. Gaddy and H. Kawai, "DYNAMIC PERFORMANCE TESTING OF DIGITAL AUDIO D/A CONVERTERS."

[20] e. technology, "What are the Drawbacks of Differential Amplifier Circuits?" https://www.eimtechnology.com/blogs/articles/what-are-the-drawbacks-of-differential-amplifier-circuits, Apr. 2024.

[21] "The Instrumentation Amplifier | Operational Amplifiers | Electronics Textbook," https://www.allaboutcircuits.com/textbook/semiconductors/chpt-8/the-instrumentation-amplifier/.

[22] T. Brown, "Design Thinking," *Harvard Business Review*, Jul. 2008.

[23] "LTC1069-7CS8#PBF," https://www.digikey.co.za/en/products/detail/analog-devices-inc/LTC1069-7CS8-PBF/889060.

[24] J. M. Fiore, "5.3: Gain-Bandwidth Product," in *Operational Amplifiers and Linear Integrated Circuits - Theory and Application (Fiore)*, May 2018.

[25] "Stabilize Your Transimpedance Amplifier | Analog Devices," https://www.analog.com/en/resources/technical-articles/stabilize-transimpedance-amplifier-circuit-design.html.

[26] T. Ebrahim, "The development of a biosensor for the early detection of pancreatic cancer," 2023.

[27] "Selecting the Right CMOS Analog Switch | Analog Devices," https://www.analog.com/en/resources/design-notes/selecting-the-right-cmos-analog-switch.html.

[28] "WEBENCH-CIRCUIT-DESIGNER Design tool | TI.com," https://www.ti.com/tool/WEBENCH-CIRCUIT-DESIGNER.

[29] M. Wilson, L. Cowie, V. Farrow, M. Cree, and J. Scott, *Simulating Fractional Capacitors with the SPICE Circuit Simulator*, Sep. 2023.

[30] "Filter manual," http://ltspicegoodies.ltwiki.org/FilterManual.php#FIR_examples.

[31] "PGA113 Pspice model - Logic forum - Logic - TI E2E support forums," https://e2e.ti.com/support/logic-group/logic/f/logic-forum/1178762/pga113-pspice-model, Dec. 2022.

[32] "What Are the Basic Guidelines for Layout Design of Mixed-Signal PCBs? | Analog Devices," https://www.analog.com/en/resources/analog-dialogue/articles/what-are-the-basic-guidelines-for-layout-design-of-mixed-signal-pcbs.html.

[33] H. Ma, R. W. R. Wallbank, R. Chaji, J. Li, Y. Suzuki, C. Jiggins, and A. Nathan, "An impedance-based integrated biosensor for suspended DNA characterization," *Scientific Reports*, vol. 3, no. 1, p. 2730, Sep. 2013.

[34] M. Ebadi, S. A. Mazlan, M. A. F. Johari, and M. R. Yusop, "Polypyrrole-based bovine serum albumin imprinted electrochemical sensor for clinical application," *Talanta Open*, vol. 12, p. 100510, Dec. 2025.

[35] S. E. Moulton, J. N. Barisci, A. Bath, R. Stella, and G. G. Wallace, "Studies of double layer capacitance and electron transfer at a gold electrode exposed to protein solutions," *Electrochimica Acta*, vol. 49, no. 24, pp. 4223–4230, Sep. 2004.

Appendix A

Project Planning Schedule

This is an appendix.

Appendix B

Outcomes Compliance

This is another appendix.